Performance of the KASCADE-Grande testbeam calorimeter

MASTERARBEIT
zur Erlangung des akademischen Grades
Master of Science in Physics
(M.Sc.)

dem Fachbereich Physik der
Universität Siegen

vorgelegt von
Tomaida-Roxana Lixandru

Juni 2004

Contents

Chapter 1

Introduction

1.1 Cosmic rays

In 1912 Victor Hess obtained the first definite evidence of cosmic rays. During several balloon flights he measured the ionization of the atmosphere. He noticed that compared to the ionization at sea level, the ionization measured first decreases, but from an altitude higher than 1.5 km it increases. This was clear evidence that the source of the ionizing radiation is extraterrestrial. In 1936 Victor Hess received the Noble prize for the discovery of cosmic rays [Gru00].

Cosmic rays mainly consist of protons and alpha particles. There is also a small fraction of heavier nuclei, electrons and energetic gamma quanta.

The energy range of cosmic rays extends from a few MeV up to more than 10^{20} eV. In figure 1.1 the differential energy spectrum of primary cosmic rays with an energy above 10^{11} eV, is presented. The particle flux depends on the energy according to an exponential law:

$$\frac{dI}{dE} \propto E_0^{-\delta}, \tag{1.1}$$

where δ is the differential spectral index.

Around an energy of $5 \cdot 10^{15}$ eV the spectral index changes. For energies $E_0 < 3 \cdot 10^{15}$ eV the spectral index has a value of 2.7, whereas for energies $E_0 > 5 \cdot 10^{15}$ eV it has a value equal to 3.1 [Bie01]. This is referred to as the 'knee' in the energy spectrum of cosmic rays. The origin of the 'knee' is not yet understood. Possible explanations are a change in the acceleration mechanisms or a change in the elemental composition of the cosmic rays. At an energy of $3 \cdot 10^{18}$ eV there is a second change in the spectral index back to the 2.7 value. This is called the 'ankle'. Around an energy of about $3 \cdot 10^{17}$ eV there is the 'second knee' of the spectrum.

The origin of cosmic rays and the acceleration mechanisms are not fully understood yet. Different theoretical models exist. In order to check them, the energy spectrum and the chemical composition at energies in the 'knee' region and above have to be determined.

For energies around 10 GeV the flux of cosmic rays is about 1 particle per cm^2 per second and can be directly measured by balloon or satellite experiments. Above primary energies of $5 \cdot 10^{14}$ eV, the flux of cosmic rays is too low for direct measurements, therefore ground based experiments with a large detection area and a long exposure time are

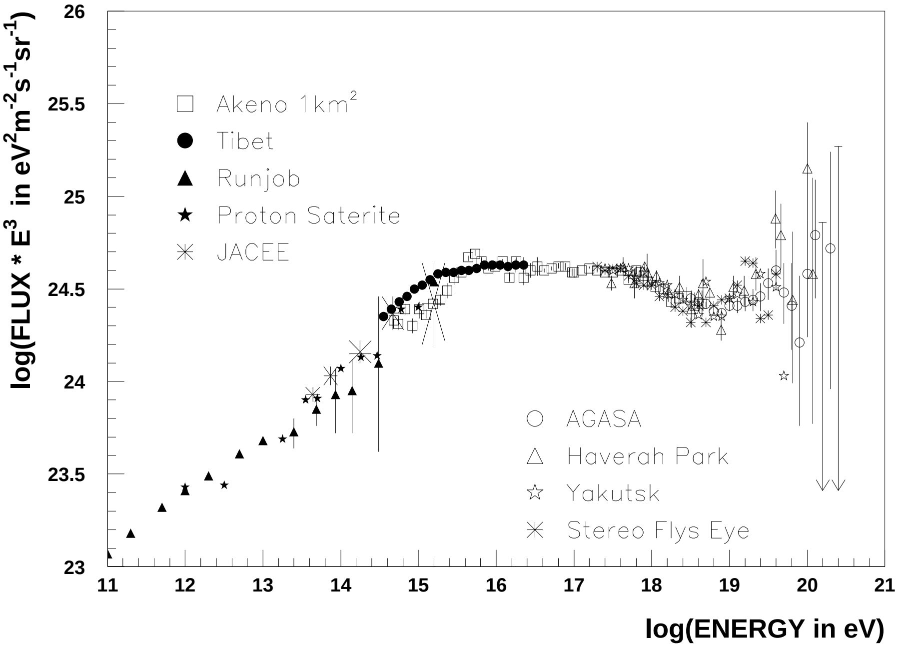

Figure 1.1: Differential energy spectrum of primary cosmic rays in an energy range from 10^{11} eV to above 10^{20} eV. For energies above 10^{18} eV results from the following experiments are shown: Haverah Park, Yakutsk, Fly's eye and AGASA. For energies below 10^{16} eV results from balloon experiments, JACEE and RUNJOB, and from Proton Satellite are shown [Nag00].

needed. The primary cosmic rays are not detected directly. Only secondary particles of the cascades, that cosmic rays initiate, are measured.

1.2 Air showers

When a primary cosmic ray particle, proton or nucleus, interacts with a nucleus in the atmosphere a part of its energy is lost in the production of secondary particles. The secondaries have enough energy to interact with the atmosphere, thus a cascade of particles, called an extensive air shower, is created. If the energy of the primary particle is high enough the shower can be detected at ground level. Most of the cascades initiated by primary particles with energies below 10^{13} eV do not reach the sea level.

In hadronic interactions mesons and baryons are created. They may decay or interact depending on their lifes times and their interaction lengths. In figure 1.2 a schematic view of an air shower is presented. It has three different components: the electromagnetic, the hadronic and the muonic component.

The hadronic component consists of pions, kaons and baryons, and they represent 1% of the total number of particles in the shower. The transverse momentum of hadrons is 0.4 GeV/c [Rao98], hence they are contained in a small area around the shower axis.

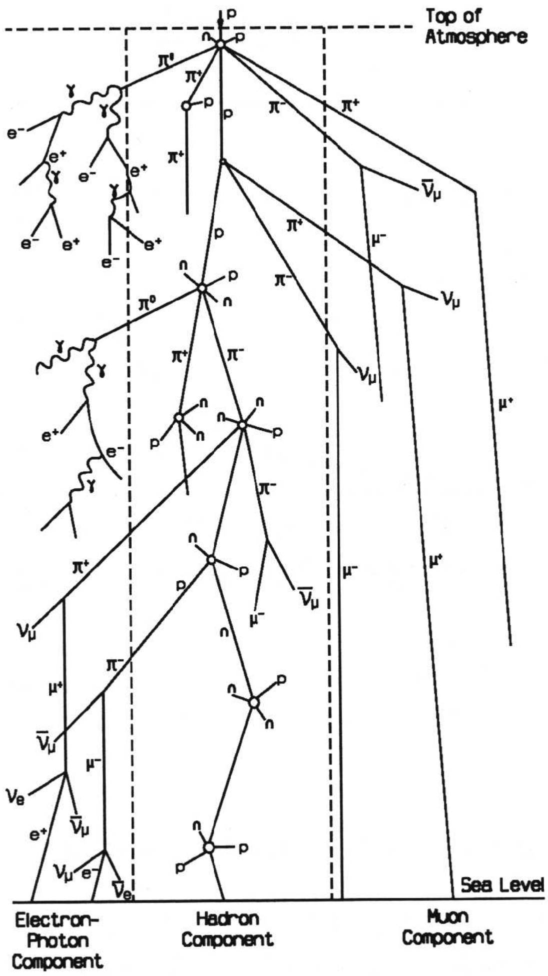

Figure 1.2: Schematic view of an extensive air shower [Gri01].

Most of the hadrons created are neutral pions. They have a very short life time ($8 \cdot 10^{-17}$ s) and in 98.8% of the cases they decay without further interactions into two photons $\pi^0 \rightarrow 2\gamma$ initiating the electromagnetic component. In 1.2% of the cases the Dalitz decay $\pi^0 \rightarrow e^+ + e^- + \gamma$ takes place. The high energy photons will create electron-positrons pairs, which in turn emit photons via bremsstrahlung. Through pair production and bremsstrahlung the electromagnetic components will continue to extend as long as the energy of the electrons is higher than the critical energy $E_c \sim 84.2\,\text{MeV}$. Below this energy ionization processes become dominant and the number of electromagnetic particles decreases. Neutral pions are continuously produced by the hadronic component. Hence, many electromagnetic subshowers are initiated.

Charged pions have a significant longer life time ($2.6 \cdot 10^{-8}$ s). A fraction of the charged pions will create more hadrons through interactions, and thus will contribute to the hadronic component. The rest will decay into muons and neutrinos, creating the muonic component of the shower. They represent 10% of the total number of particles in the shower. Muons rarely interact strongly and they lose energy mainly through ionization. Low energy muons decay into electrons and neutrinos and contribute to the electromagnetic component. The lateral spread of muons is determined by the transverse momentum of the parent pion. Hence, muons at large distances from the shower core give important information about the highest energy interactions and about the nature of the primary particle. If it has enough energy, the muon reaches the ground level.

In the interaction of a hadron with nuclei of the air a large number of secondary particles is created. The most energetic one receives about 50% of the energy of the initial hadron. Due to this high energy it will dominate the subsequent development of the shower and is called 'leading particle'.

Unaccompanied or single hadrons are events induced by cosmic rays for which only one hadron reaches the ground level. On average a particle interacts 12 times before reaching the ground and thus has less than 1% of the energy of the primary particle. Single hadrons interact only four times and they reach the ground with approximately 10% of the energy of the primary particle, thus they are stronger correlated to the energy of the primary particle, than the hadrons in the shower.

The hadron calorimeter in the KASCADE-Grande experiment is intended to measure single hadrons and to determine their energies and directions.

1.3 Scope of this thesis

In order to obtain a data-based energy calibration of the hadron sampling calorimeter in the KASCADE-Grande experiment, a testbeam calorimeter has been built and tested. In this thesis the performance of the testbeam calorimeter is studied. The acquired data are analyzed and the results are presented.

- In chapter 2 the components of the KASCADE-Grande experiment are described. The central detector and the hadron calorimeter are described in more details, since they are related to the topic of this thesis.

- In chapter 3 the basics of hadron calorimetry are presented and the need of a calibration in a testbeam is explained.

- In chapter 4 the setup of the testbeam calorimeter is described in detail. The use of liquid ionization chambers and its advantages are discussed and a summary of the data taken during the testbeam is also presented.

- Chapter 5 covers the data analysis. For each step in the analysis the procedure is explained and results are presented.

- In chapter 6 a summary is given.

Chapter 2

The KASCADE-Grande experiment

KASCADE-Grande is an extensive air shower experiment, located on the site of the Forschungszentrum Karlsruhe in the Rhine valley, at 110 m a.s.l. (49° northern latitude, 8° eastern longitude). Its aim is to determine the primary energy spectrum and the mass composition of cosmic rays in the energy range from $3 \cdot 10^{14}$ eV to 10^{18} eV. The particle flux at high energy is very low. To investigate cosmic rays in this energy range, a ground based detector, that ensures a large detection area and a large exposure time, must be used. The KASCADE-Grande experiment was built to fulfill these conditions. It includes the KASCADE array, the muon tunnel, the central detector with the hadron calorimeter, the Grande and Piccolo arrays.

2.1 The KASCADE setup

The KASCADE (KArsruhe Shower Core and Array DEtector) experiment started taking data in 1996. It uses different detector systems to simultaneously detect all three components (electromagnetic, muonic and hadronic) of an extensive air shower (EAS), measuring several observables for each single event. The electromagnetic component is detected using an array of scintillation detectors plus the top layers of liquid ionization chambers and plastic scintillators in the calorimeter. In order to measure the muonic component at four different thresholds, scintillators and tracking chambers are used. For the hadronic component, the hadron sampling calorimeter in the central detector is used. A summary of all detector components, their sensitive areas and energy thresholds is given in table 2.1.

- The *KASCADE array* has a detection area of $200 \times 200\,\mathrm{m}^2$ (see figure 2.1). Its aim is to measure the particle densities and the arrival times of electrons, photons and muons. It consists of 252 scintillation detector stations placed on a square grid of 13 m spacing. The array is electronically divided in clusters of 16 detector stations. The inner four clusters have only 15 stations. This is due to the absence of four stations in the middle of the array, as this place is occupied by the central detector. The stations in the outer 12 clusters are equipped with e/γ detectors (5 cm liquid scintillators) and a muon detector (3 cm plastic scintillators). Between the two kinds of detectors, a lead/iron absorber plate corresponding to

Detector	Particle	Total area $\left[\mathrm{m}^2\right]$	Threshold
KASCADE:			
Array, liquid scintillators	e/γ	490	5 MeV
Array, plastic scintillators	μ	622	230 MeV
Muon tracking detector, streamer tubes	μ	128 × 4 layers	800 MeV
central detector:			
Calorimeter, liquid ionization chambers	h	304 × 8 layers	50 GeV
Trigger layer, plastic scintillators	μ	208	490 MeV
Top cluster, plastic scintillators	e/γ	23	5 MeV
Top layer, liquid ionization chambers	e/γ	304	5 MeV
Multi-wire proportional chambers	μ	129 × 2 layers	2.4 GeV
Limited streamer tubes	μ	250	2.4 GeV
Grande	e/μ	370	3 MeV
Piccolo	e/μ	80	5 MeV

Table 2.1: Summary of the KASCADE-Grande detector components, their total sensitive areas and thresholds for vertical particles [Kam03, Ant03].

20 attenuation lengths is placed, used to stop the electromagnetic component of the shower. The stations in the inner four clusters do not have a muon detector. Whenever a coincident signal of at least five stations in a cluster happens, a trigger is received. This is the main trigger for KASCADE and it corresponds to a threshold in the order of 10^{14} eV. A second trigger is generated by the trigger layer in the central detector. The array allows for a total detection area of $490\,\mathrm{m}^2$ with an energy threshold of 5 MeV for e/γ and $622\,\mathrm{m}^2$ and a threshold of 230 MeV for muons [Ant03].

- The *central detector* is placed in the middle of the array and it has a total area of $320\,\mathrm{m}^2$. The setup is shown in figure 2.2.
  - The *hadron calorimeter* [Eng99]. For determining the primary particle initiating an air shower, the hadron shower content plays an important role. That is why the main component of the central detector is a hadron sampling calorimeter. The aim of the calorimeter is to measure single hadrons and to determine their energies and directions. To accomplish this, a fine lateral segmentation is needed. As shown in figure 2.2 the calorimeter comprises: one lead absorber layer of 5 cm thickness used to filter the electromagnetic component of the shower, 8 layers of iron absorber, with thicknesses increasing from 12 cm in the upper part to 24 cm and 36 cm in the lower part, 9 layers of liquid ionization chambers and one layer of concrete absorber 77 cm thick. Due to the different sampling from top to bottom, the energy resolution scales as $\sigma(E)/E$ and not as $\sigma(E)/\sqrt{E}$, and it varies from 20% at 100 GeV to 10% at 10 TeV. In total there are 10000 liquid ionization chambers (40000 read-out electronic channels) representing the active elements of the calorimeter. The room temperature liquids tetramethylpentane (TMP) and tetramethylsilane (TMS) are used as dielectric medium. This is the first large scale calorimeter

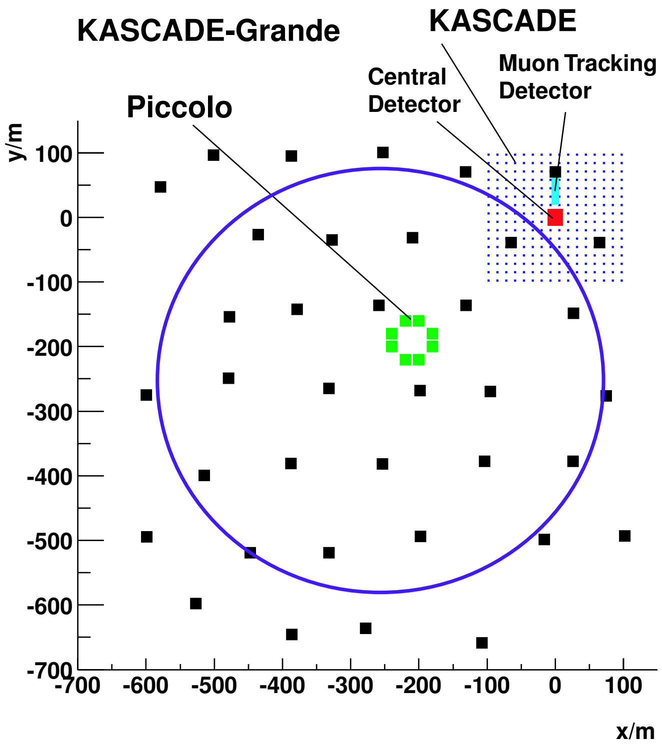

Figure 2.1: Schematic view of the KASCADE-Grande experiment [Kam03]

which uses a warm liquid technique. The main reason for using liquid ionization chambers is long-term stability and a large dynamic range. A more detailed description of liquid ionization chambers will be given in chapter 3. Seven of the liquid ionization chamber layers are placed in-between the iron absorber layers. One is placed on top of the lead layer and one below the concrete absorber, acting as a tail catcher. The total depth of the calorimeter corresponds to 11.5 nuclear interaction lengths for vertical protons, which ensures a shower containment of 97.5 % up to 25 TeV [Ant03].

- The *top layer* of liquid ionization chambers is used to study the shower core more precisely. The chambers are filled only with TMP. In order to be able to separate the minimum ionizing particles from the noise, the thickness of the liquid is twice as large as in the chambers in the other layers.
- On top of the calorimeter 25 scintillation counters are placed covering 7.5% of the area. This is the *top cluster* layer and is used as a trigger for small extensive air showers and for the investigation of the electromagnetic cores of air showers, compensating in this way for the four missing stations in the center of the array.
- The *trigger layer*. Below the third iron absorber layer, where showers of 100 GeV hadrons deposit the maximum energy, 456 scintillation counters are placed on 2/3 of the calorimeter area. They are used for the reconstruction of the arrival time and for triggering both the liquid ionization chambers and the muon detectors. Two kinds of trigger conditions are used to collect data:

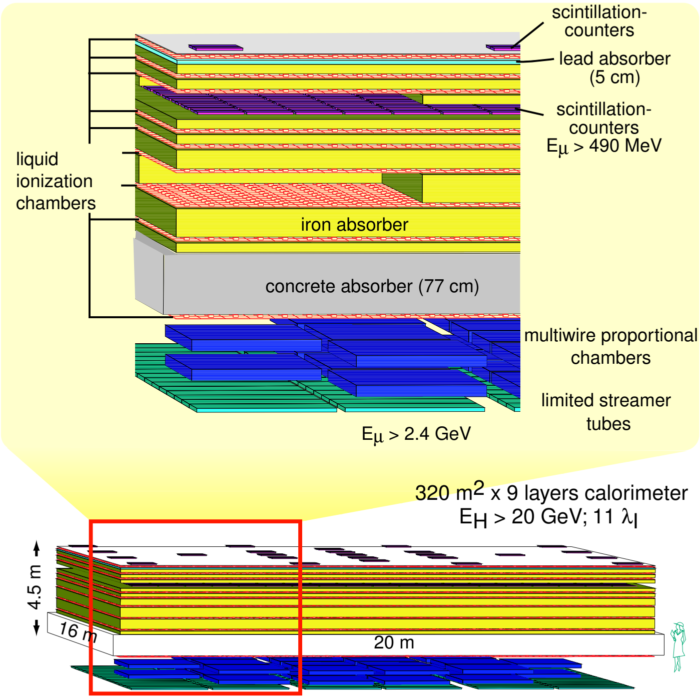

Figure 2.2: Schematic view of the KASCADE central detector [Ant03]

the muon trigger and the hadron trigger. The muon trigger is generated when at least eight scintillators show a signal larger than 1/3 of a passing muon signal. The hadron trigger is generated when at least one scintillator shows a signal larger than a signal corresponding to 50 passing muons.

- Below the hadron calorimeter two layers of *multi-wire proportional chambers* (MWPC) and a layer of limited streamer tubes are placed. They are used to measure high energy muons, with a threshold of 2.4 MeV for vertical muons.

The aim of the calorimeter is to measure single hadrons and to separately determine their energies and directions. The main issue concerning the calorimeter is to obtain a data-based calibration. For this reason a testbeam calorimeter was built and tested at CERN in 2003. The setup of the testbeam calorimeter will be presented in the third chapter and the results of the data analysis in the fourth chapter.

- The *muon tracking detector* (MTD) is placed north of the central detector in a $5.4 \times 2.4 \times 44\,\mathrm{m}^3$ tunnel and it measures muons with energies larger than 0.8 GeV. The energy threshold is given by the shielding of 18 radiation lengths, made out of concrete iron and soil. Inside the tunnel, positional sensitive limited streamer tubes are placed in three horizontal layers with a vertical spacing of 82 cm. This ensures a geometrical resolution of 0.35° for vertical muons [Dol02]. There are also two vertical layers of streamer tubes placed along the sides, used to measure the inclined tracks. The counting gas used is a mixture of 20% CO_2, 20% argon and 60% isobutane. This ensures a three-hit track efficiency of 60% [Ant03].

2.2 The Grande array

Two other arrays were added to the KASCADE experiment. The Grande array was added in order to increase the detection area to $0.5\,\mathrm{km}^2$ and the energy range to 10^{18} eV. The Piccolo array was added to obtain a better trigger system.

The *Grande array* consists of 37 stations situated on a hexagonal grid of 130 m spacing and has a total detection area of $0.5\,\mathrm{km}^2$. Each detector station is equipped with 16 plastic scintillators, with an area of $80 \times 80\,\mathrm{cm}^2$ and a thickness of 4 cm each. All scintillators are connected to photomultipliers. The 12 outer scintillators work only at high gain and are used to measure low particle densities. The four inner ones work also at low gain and are used for high particle density measurements. Electronically the array is divided into 18 hexagons. Each hexagon is composed of six outer stations and a central one. Whenever a four-fold coincidence occurs (central station plus three other), an internal trigger is generated. The Grande array also obtains an external trigger from the central KASCADE-Grande trigger distributor, i.e. from Piccolo and all KASCADE components.

2.3 The Piccolo Trigger Array

The *Piccolo Trigger Array* is an eight stations array. It is situated between the center of the KASCADE array and the center of the Grande array. Each detector station is equipped with 2 modules of 6 plastic scintillation plates, hence a sum of 12 scintillators each with an area of $310 \times 30\,\mathrm{cm}^2$ [Chi03]. The Piccolo array is mainly used to provide an external trigger for KASCADE and the Grande array. In this way data can be collected from all KASCADE-Grande detectors. Using the Piccolo array, a full detection efficiency for energies $E > 10^{16}$ eV can be accomplished, whereas its absence limits the full detection efficiency to energies greater than 10^{17} eV [Kam03].

Chapter 3

Hadron calorimetry

Calorimeters are blocks of detector material equipped with readout electronics. They allow particle detection and measurements of different properties of the particles. Usually the particle energy is measured, but it is also possible to measure the position of the particle and even use calorimeters for triggering. An incoming particle will interact with the material through electromagnetic and hadronic processes and will produce a cascade of particles called shower. If the material is thick enough, then the shower will be fully contained and the initial particle will lose all of its energy in the volume of the calorimeter. During these processes the medium is excited or heated up, hence the name calorimeter.

There exists a great variety of calorimeters. The choice of one type over another depends mainly on two factors: the physics of interest and the cost involved. The thickness of the calorimeter is a very important factor for the shower containment, and thus for the physics, and it strongly influences the costs. For a good energy resolution, in order to avoid fluctuations due to particles escaping the detection area, usually a shower containment of 95% is required. Therefore the depth of the calorimeter should be chosen accordingly. A hadronic shower goes much deeper and is much broader than an electromagnetic one. This means that deeper calorimeters are needed to study hadronic showers. The same depth for the study of electromagnetic showers would imply unjustified additional costs. In addition, the choice of the material used will differ, since a material with a larger interaction length is needed in the case of hadronic showers. Also the segmentation of the calorimeter depends a lot on the physics processes to study. A much finer segmentation is required for electromagnetic showers.

Therefore, calorimeters are traditionally separated depending on the type of the particles that have to be measured, in electromagnetic and hadronic calorimeters. *Electromagnetic* calorimeters are used to measure electrons, positrons and photons while *hadron* calorimeters are used to measure mostly hadrons.

Calorimeters can also be classified in homogeneous and sampling calorimeters, according to how they are constructed. *Homogeneous* calorimeters consist of only one type of material which is sensitive to the particles and that contributes to the signal generation. *Sampling* calorimeters are made up of alternating layers of active and passive materials. Only the fraction of energy deposited in the active material of the calorimeter can be measured in form of a signal, which can be light or charge. The amount of energy deposited depends on the energy of the particle. For the passive layers usually high density material are used, e.g iron, copper or lead.

Both types have advantages and disadvantages (see section 3.3).

There are several characteristics that make calorimeters attractive to cosmic ray and accelerator based experiments [Fab85, Fab03].

- Calorimeters are sensitive to both charged and neutral particles.
- An incoming particle interacts with the calorimeter and starts a shower. The number of resulting secondary particles (N) is directly proportional to the energy of the particle, and the uncertainty in the energy resolution depends on the statistical fluctuation of N. For the energy resolution follows:

  $$\frac{\sigma(E)}{E} = \frac{\sqrt{N}}{N} \propto \frac{1}{\sqrt{E}}. \tag{3.1}$$

  This means, that the energy resolution of a calorimeter improves with the energy of the incoming particle. This fact makes calorimeters suitable for high energy particle physics.
- Although initially intended for energy measurements, calorimeters can also be used to identify particles since they give different responses depending on the type of particles: electrons, muons and hadrons.
- Using finely segmented calorimeters, the position and angle of the incoming particle can also be measured.
- The length needed for sufficient containment increases logarithmically with the energy of the incident particle, and this makes calorimeters cost-effective.
- Depending on the detection technique employed, calorimeters can generate fast time responses which means that they can also be used for trigger purposes.

3.1 Energy loss in matter

Interaction of charged particles

Relativistic charged particles interact with matter mainly through ionization. The mean rate of energy loss is parameterized by the Bethe-Bloch formula:

$$-\frac{dE}{dx} = 2\pi N_A r_e^2 m_e c^2 \rho z^2 \frac{Z}{A}\frac{1}{\beta^2}\left[\ln\frac{2m_e c^2\gamma^2 T_{max}}{I} - 2\beta^2 - \delta\right], \tag{3.2}$$

where z is the charge of the incident particle, Z and A are the atomic and mass numbers of the absorber, m_e is the electron mass, r_e is the classical electron radius, N_A the Avogadro number and I is the ionization constant which can be approximated for $Z > 1$ by $I = 16\ Z^{0.9}\,\text{eV}$.

δ describes the density effect. At high energies of the incoming particle its electric field flattens and extends. Due to this relativistic effect distant collisions will also contribute to the energy loss. However the extension of the field is limited by the polarization of the medium. As a result the contribution of outer electrons is reduced. The denser the material, the more important the density effect becomes.

T_{max} is the maximum energy transferred in a single collision and is given by:

$$T_{max} = \frac{2m_e\gamma^2\beta^2}{(\frac{m_e}{M})^2 + 2\gamma\frac{m_e}{M} + 1}, \tag{3.3}$$

where M is the mass of the incident particle, $\beta = \frac{v}{c}$ and the Lorentz factor is given by $\gamma = \frac{1}{\sqrt{1-\beta^2}}$.

At energies larger than 100 MeV, electrons and positrons will also lose energy through bremsstrahlung:

$$e^- + \text{nucleus} \rightarrow e^- + \text{nucleus} + \gamma \ . \tag{3.4}$$

Due to the Coulomb field of the nucleus the particles are decelerated and they lose a fraction of their energy by emitting photons.

For high energy muons, another process is more important than bremsstrahlung. That is electron-positron pair production via virtual photons in the Coulomb field of the nuclei (μ + nucleus $\rightarrow \mu + e^+ + e^-$ + nucleus). Up to energies around 100 MeV muons lose energy through ionization and high-energy recoil electrons, called δ-rays.

Photon interactions

Photons interact with matter through four processes [Wig00]: photoelectric effect, pair production, Rayleigh scattering and Compton scattering. The dominant process depends both on the energy of the photon and on the electron density of the medium.

- In the *photoelectric effect* the photon will transfer all its energy to an atomic electron. If the energy received is high enough (higher than the binding energy), the electron will be liberated. Its place in the atom shell will then be filled by another electron from a higher shell. The energy, equal to the difference between the energy of the two shells, is either liberated by emitting X-rays or is transferred to another electron (Auger electron). The cross section for the photoelectric effect is proportional to Z^4 and E^{-3}, which means it is important only at low energies, depending on the atomic number of the material.

- The *Rayleigh scattering* process is important at low energies. The photon is scattered by the atomic electrons without losing energy. So this process only influences the spatial distribution of the energy.

- In the *Compton scattering* process the photon is scattered by quasi-free atomic electrons. Except in high Z materials, this is the most probable process for photons with energies from a few keV to 5 MeV. The cross section for Compton scattering decreases with energy as $1/E$.

- If the energy of the photon is high enough (larger than twice the electron rest mass) then *pair production* occurs:

  $$\gamma + nucleus \rightarrow e^+ + e^- + nucleus \ . \tag{3.5}$$

  Electron-positron pairs are created in the Coulomb field of the nucleus. The resulting electron will be absorbed by an ion and the positron will annihilate with an electron. The cross section for pair production increases with energy.

For energies between 5 and 20 MeV photonuclear reactions (e.g. γn, γp) can play a role, but the cross section for such processes is less than 1% of the total cross section.

Interactions of neutrons

The nuclear process through which neutrons interact with matter depends strongly on the energy of the neutron [Leo87].

- In the range from a few eV to 1 MeV the dominant process is *elastic scattering* from nuclei (i.e. $A(n,n)A$).
- If the neutron has enough energy to excite the nucleus ($\sim 1\,\mathrm{MeV}$), inelastic scattering takes place (e.g. $A(n,n^{'})A^{*}$, $A(n,2n^{'})B$). The excitation energy is then released in form of one or more photons.
- If the neutron loses all its kinetic energy in collisions with the material, it can either decay or be captured by an atomic nucleus. The latter is more probable. In this way the binding energy lost when the neutron was released, is regained. The resulting compound nucleus will emit this excess energy as γ-rays. Therefore the process is called *radiative neutron capture* (i.e. $n + (Z,A) \to \gamma + (Z, A+1)$).
- In the eV to keV region several nuclear processes may occur in which the neutron is captured and charged particles are emitted: $(n,p), (n,d), (n,\alpha), (n,t), (n,\alpha p)$.
- At thermal energies fission can occur (i.e (n,f)).
- From neutrons with energies larger than 100 MeV hadron showers can be produced.

3.2 Shower development

Electromagnetic showers

As mentioned in the previous section, the dominant interaction process of particles with matter depends on the energy of the particle. At high energies (in the GeV range) the combined effect of pair production from photons and bremsstrahlung for electrons is called an electromagnetic shower. From these interactions secondary particles result, photons for bremsstrahlung and electrons and positrons from pair production. The secondary particles will in turn produce other particles, thus creating a particle shower. The multiplication process continues as long as the energy of the electron component is higher than the critical energy. The critical energy E_c is the energy at which the energy losses through radiation equal the energy losses by ionization. For materials with $Z \geq 13$ the critical energy is given by:

$$E_c = \frac{550\,\mathrm{MeV}}{Z}. \tag{3.6}$$

The longitudinal and lateral developments of an electromagnetic shower can be described in terms of the radiation length, which is parameterized as:

$$X_0 = \frac{716\ A}{Z(Z+1)\ln(287/\sqrt{Z})}\left[\frac{\mathrm{g}}{\mathrm{cm}^2}\right], \tag{3.7}$$

where Z and A are the atomic and mass numbers of the material, respectively. Values of the radiation lengths for different absorber materials can be found in table 4.1.

Material	Z	$\rho\,\left[\frac{\mathrm{g}}{\mathrm{cm}^3}\right]$	E_c [MeV]	$X_0\,\left[\frac{\mathrm{g}}{\mathrm{cm}^2}\right]$	X_0/ρ [cm]	R_M [cm]	$\lambda_{had}\,\left[\frac{\mathrm{g}}{\mathrm{cm}^2}\right]$	λ/ρ[cm]
Pb	82	11.35	7.40	6.37	0.56	1.7	194.0	17.09
Fe	26	7.87	20.7	13.84	1.76	1.78	131.9	16.75
Cu	29	8.96	18.8	12.86	1.43	1.5	134.9	15.05
TMP (C_9H_{20})	74	0.7195	7.43	0.026	0.037	0.1045	56.88	79.054

Table 3.1: Critical energies, radiation lengths X_0 and nuclear interaction lengths λ_{had} for a few materials often used in calorimetry [Gro00]. The critical energies and the Molière radius R_M were calculated using formulas (3.6) and (3.12).

For electrons the radiation length X_0 gives the average path distance $x = X_0$ for an electron to reduce its energy, via bremsstrahlung, to $1/e$ of its initial energy E_0.

$$E(x) = E_0\; e^{(-x/X_0)}. \tag{3.8}$$

In contrast to electrons, photons will reduce their intensity to $1/e$ of their initial intensity I_0, via pair production, after a distance of $x = \frac{9}{7}X_0$

$$I(x) = I_0\; e^{-(7/9)(x/X_0)}. \tag{3.9}$$

This means that the shower development for both, electrons and photons, has the same scale, so that electromagnetic showers can be described by the radiation length. The position of the shower maximum (the point where the multiplication process stops) is given by [Fab85]:

$$t_{max}[X_0] \simeq \ln\frac{E_0}{\varepsilon} + t_0\ , \tag{3.10}$$

with ε being the energy of the incoming particle and t_0 equal to -0.5 for electrons and to 0.5 for photons. This shows that the length of the shower increases logarithmically with the energy. The thickness of a calorimeter should be chosen accordingly. To obtain 98% containment of the shower, for an energy of the initial particle from 10 to 1000 GeV, the thickness should be equal to:

$$L(98\%) \simeq 2.5\ t_{max}\ X_0\ . \tag{3.11}$$

The lateral development of the electromagnetic shower is given by multiple scattering of electrons and positrons but also by photons emitted by these electrons/positrons through bremsstrahlung. The transverse size of the shower is given by the Molière radius, which is a measure of the lateral deflection of electrons of energy ε, after passing through one radiation length of material. The Molière radius is given by:

$$R_M\ \left[\mathrm{g/\,cm}^2\right]) = \frac{21\,\mathrm{MeV}}{\varepsilon\,[\mathrm{MeV}]}X_0\ . \tag{3.12}$$

90% of the energy of a shower is contained in a cylinder with a radius $\sim 1\ R_M$.

Hadronic showers

On one hand, hadronic interactions with the calorimeter material result in the production of energetic hadrons. On the other hand, a significant part of the initial energy is lost in nuclear processes like excitation, nuclear evaporation and spallation. Due to inelastic processes secondary particles are produced: charged and neutral pions, neutrons, protons, kaons, etc. Some of the particles produced, mainly π^0's and η's, will quickly decay into two photons: $\pi^0, \eta \rightarrow \gamma\ \gamma$. The photons will interact electromagnetically with the material as described earlier. This means, that hadron showers also have an electromagnetic component. Approximately, one third of the pions produced are neutral pions, but the fraction of the initial energy that goes to this electromagnetic component has large and non-Gaussian event to event fluctuations.

Compared to electromagnetic showers where the energy of electrons and photons is completely detectable, in hadronic showers a considerable fraction of the energy is 'invisible'. There are several reasons for the decrease of the visible energy.

- As mentioned before, a certain part of the hadron energy is used to break-up the nuclear bonds, and the energy needed, i.e. the nuclear binding energy, will not contribute to the visible energy.
- In sampling calorimeters, the nuclear fragments, that result from the break-up of nuclear bonds, do not arrive at the active layers.
- Long lived particles, e.g. neutrons or K^0_L, can leave the calorimeter volume without any contribution to the detected energy.
- Certain particles like pions and kaons can decay into muons, which will deposit only a small part of their energies in the calorimeter.

Due to this great variety of processes that contribute to the invisible energy, there are large fluctuations in the energy measurements. Hence, the energy resolution of hadronic calorimeters will typically be worse compared to electromagnetic calorimeters.

The ratio between the calorimeter's responses to the electromagnetic and hadronic component is called the e/h ratio. If $e/h = 1$ the calorimeter is called compensating, if $e/h > 1$ non-compensating. Experimentally, the e/h response can not be obtained directly. Therefore, it has to be determined from the e/π ratio [Wig00]:

$$e/\pi = \frac{e/h}{1 - f_{em}[1 - e/h]}, \tag{3.13}$$

where f_{em} is the fraction of the electromagnetic component. For an accurate result the e/π ratio should be measured for an energy range as large as possible.

Unlike homogeneous calorimeters, which are intrinsically non-compensating, compensation can be achieved for sampling calorimeters. However, most hadron calorimeters are non-compensating. There are two general methods to achieve compensation. One way is to reduce the electromagnetic component and the second method is to increase the hadronic response. A reduced response to the electromagnetic component can be archived using high Z absorber material. A further reduction is achieved by shielding the active layers by passive low-Z materials. For the increase of the hadronic response an important role is played by the calorimeter response to soft neutrons. Neutrons resulting from nuclear interactions can induce fission and produce more energy in the form of other neutrons and energetic γ-rays which, if recorded, can enhance the hadronic signal. In uranium calorimeters the nuclear fission is an important source of neutrons and energetic photons. Using ^{238}U as absorber material, an energy of $E \sim 200\,\mathrm{MeV}$ is released in each fission process, out of which 90% is transfered to the fission fragments (and does not contribute to the detected signal) but the remaining 10% can contribute to the visible energy [Wig00]. The photons can be recorded by choosing an appropriate sampling calorimeter and the neutrons through the recoil protons they produce in (n, p) reactions. The active readout material also plays an important role in compensation. Hydrogen is very efficient in thermalizing neutrons, thus it plays an important role for the (n, p) reactions (which occur at low energies). The resulting recoil protons deposit almost all their energy in the active layers. Therefore they directly contribute to the signal. This is why materials with a high concentration of hydrogen are often the preferred choice for the active layers. Compensation was also attempted using Fe/TMP and Pb/TMP sampling calorimeters [Aub93]. The hadronic signal can also be enhanced by increasing the signal integration time, since neutrons and photons can be delayed.

The shower profile of a hadronic shower can be described in terms of the nuclear interaction length:

$$\lambda_{had} = \frac{A}{N_A \ \rho \ \sigma_{inel}}, \tag{3.14}$$

with A – mass number of the absorber,
N_A – Avogadro number,
ρ – density of the absorber,
σ_{inel} – inelastic cross section .

The position of the shower maximum can be approximated by:

$$t_{max} \simeq \left(0.2 \ \ln\left(\frac{E_0}{\mathrm{GeV}}\right) + 0.7\right) \cdot \lambda_{had}, \tag{3.15}$$

and the approximate shower depth for 95% longitudinal containment reads:

$$L_{0.95} \simeq t_{max} + 2.5\lambda_{had} \left(\frac{E_0}{\mathrm{GeV}}\right)^{0.13}. \tag{3.16}$$

The lateral profile of a hadronic shower consists of a narrow core surrounded by a halo. The core is given by the electromagnetic component of the shower. The halo is given by the hadronic component and exhibits an exponential decrease from the shower's axis. A cylinder with a radius equal to λ_{had} will ensure a 95% lateral containment.

3.3 Sampling vs. homogeneous calorimeters

Homogeneous calorimeters

The main advantage of homogeneous calorimeters is the excellent energy resolution that they can achieve. This is due to the fact that the entire volume is sensitive to the particles and the whole energy of the particle is deposited in this active medium. On the other hand, they have two main drawbacks. First, they can not be easily segmented, thus they are not suited for position measurements or particle identification. Second, they are non-compensating and suitable materials have large interaction lengths. This is why they are seldomly employed as hadron calorimeters in accelerator experiments.

They are however used in neutrino and astroparticle physics experiments in which, for the detection of rare events, large volumes of inexpensive materials are needed (like air or water).

Sampling calorimeters

Compared to homogeneous calorimeters sampling calorimeters have worse energy resolution. Only a small fraction, typically a few percents or less [Fab03], of the total energy of the incident particle is deposited in the active layers and contributes to the detected signal. Therefore the sampling fluctuations caused by the absorber layers reduce the energy resolution. For electromagnetic sampling calorimeters the energy resolution will typically be in the range [Fab03]:

$$\frac{\sigma(E)}{E} \sim \frac{5\ -\ 20\%}{\sqrt{E\,[\,\mathrm{GeV}]}}, \tag{3.17}$$

and for hadron sampling calorimeters the best energy resolution that can be achieved (e.g. for uranium-scintillator or uranium-liquid-argon calorimeters) is [Wig00]:

$$\frac{\sigma(E)}{E} \approx \frac{35\%}{\sqrt{E\,[\,\mathrm{GeV}]}}. \tag{3.18}$$

Unlike homogeneous calorimeters, sampling calorimeters can easily be segmented both longitudinally and transversely so they can achieve better spatial resolution and particle identification than homogeneous calorimeters. Almost all hadron calorimeters are sampling calorimeters. This is mainly due to the fact that they can provide enough interaction lengths in a thickness of typically less than 2 m [Fab03]. Moreover, the energy resolution of hadronic showers is limited by the e/h fluctuations and not by the sampling fluctuations.

For electromagnetic sampling calorimeters the radiation length is given by:

$$X_0 = \frac{1}{\sum_{i=1}^{N} f_i/X_0^i}, \tag{3.19}$$

and the Molière radius by:

$$R_M = \frac{21\,\mathrm{MeV}}{\sum_{i=1}^{N} f_i E_c^i/X_0^i}. \tag{3.20}$$

The f_i's are the volume fractions of the different layers, E_c^i's denote the critical energies and X_0^i's the radiation lengths of the different materials i.

3.4 Energy resolution

The energy resolution is considered to be the most important feature of a calorimeter. Charged particles are generated in the shower and deposit energy. A part of the energy deposited in the active layers is transformed into a measurable signal. The energy resolution gives the precision, with which this energy is measured and can be parameterized as the quadratic sum of three terms:

$$\frac{\sigma(E)}{E} = \frac{a}{\sqrt{E}} \oplus b \oplus \frac{c}{E}. \tag{3.21}$$

- The *sampling term a* includes the Poissonian statistical fluctuations in the shower development, i.e. fluctuations in the number of secondary particles, and it has a $1/\sqrt{E}$ dependence as shown in formula (3.1). For sampling calorimeters it also includes sampling fluctuations. As mentioned before, only the energy deposited in the active layers of the calorimeter, which is a small fraction of the total energy of the particle, will contribute to the detected signal. This fraction depends on the number N_L of layers in the calorimeter:

  $$\frac{\sigma(E)}{E} \propto \frac{1}{\sqrt{N_L}}. \tag{3.22}$$

  If the thickness of the passive layers is large compared to the thickness of the active layers ($d_{passive} \gg d_{active}$), N_L is approximately given by the ratio between the length of the calorimeter and the thickness of the absorber plates:

  $$N_L = \frac{L}{d}. \tag{3.23}$$

  Therefore the energy resolution will be proportional to the square root of the absorber thickness:

  $$\frac{\sigma(E)}{E} \propto \sqrt{d}. \tag{3.24}$$

  The thickness of the active material can also give rise to fluctuations. If the active layer is very thin, there are fluctuations in the number of ionization processes. In this case (for example for gaseous media) Landau and path-length fluctuations become important. The sampling fluctuations represent the main contribution to the energy resolution of electromagnetic sampling calorimeters.

- The *constant term b* is energy independent and dominates the energy resolution at high energies. It includes fluctuations due to calibration errors or incomplete shower containment.

- The *noise term c* describes the statistical fluctuations in the energy resolution due to electronic noise, meaning the event to event fluctuation of the charge collected in the absence of a shower. It varies as E^{-1}.

Some authors use a linear sum to add the sampling and constant term. This is only correct, if there is a strong correlation between the contributions to these terms. Otherwise a quadratic sum should be used [Gro00]. There is even a third alternative which suggests an energy dependence of the 'constant' term [Wig00].

Experimentally the energy resolution is determined from the accuracy, with which the energy of a particle of a known energy is measured by the calorimeter.

3.5 Calibration of a calorimeter

In order to obtain a good energy resolution, a proper calibration is essential. The main calibration procedures are the hardware calibration and the calibration of the device in a testbeam.

- The hardware calibration is used to adjust the cell-to-cell response of the detector. To achieve this, a known pulse is injected at the input of the readout chain and the output signal is read out. A good hardware calibration reduces the contribution to the constant term of the energy resolution.

- The testbeam calibration gives the relation between the signal measured by the readout electronics and the energy deposited by an actual particle traversing the detector. In other words, calibration constants, that give a relation between the units of the recorded calorimeter signal and energy units, must be determined. Experimentally, testbeam studies are performed with monoenergetic particles like muons and electrons. This method results in high statistical precision but it also leads to systematic mismeasurements of the energy.

  - The calorimeter gives different responses depending on the type of the incident particle, therefore the calibration constants also depend on the type of the particle. That is why calibration constants obtained for a particular type of particle in a testbeam measurement will introduce a certain error when used for other types of particles.
  - The response of the calorimeter also depends on the energy of the particle. Therefore, the calibration constants obtained for particles with certain energies will introduce errors when used for particles with other energies.
  - Another source for a mismeasured energy is the shower size. There is a great variety of particles in a shower leading to many different shower shapes. For example, electrons and positrons in the electromagnetic shower component are concentrated close to the shower axis, while the neutrons in the hadronic shower component will go much deeper into the material, in both longitudinal and lateral directions. Therefore the energy deposited in the regions far from the shower axis is caused almost exclusively by these neutrons. Hence using calibration constants obtained from muon or electron testbeams will lead to mismeasurements of the energy in calorimeter segments far away from the shower axis.

Chapter 4

The testbeam experiment

In order to test and verify the energy calibration of the KASCADE-Grande hadron sampling calorimeter, a testbeam calorimeter was built and tested at CERN in 2003. The testbeam calorimeter consists of spare modules of the original KASCADE calorimeter and is described in detail later in this chapter. The acquired data are analyzed in this thesis.

4.1 Setup of the testbeam calorimeter

The setup of the testbeam calorimeter is similar to the longitudinal structure of the KASCADE-Grande calorimeter. Only the number of layers and the thickness of the absorber material are different. Instead of nine layers of liquid ionization chambers there are 15, and instead of eight layers of iron absorber there are 13. As shown in figure 4.1 the calorimeter consists of:

- 15 layers of liquid ionization chambers, representing the active elements of the calorimeter, each layer having an area of $1 \times 1\,\mathrm{m}^2$,
- 13 layers of iron absorber placed in-between the active layers, starting behind the second active layer, each 10 cm thick,
- a 5 cm layer of lead absorber which is installed between the first and the second layer of liquid ionization chambers.

Between every two consecutive layers of liquid ionization chambers there is a spacing of 19.5 cm. The total length of the calorimeter adds up to approximately 270 cm, which corresponds to 8.6 nuclear interaction lengths for protons.

4.2 The ionization chambers

4.2.1 Structure of the ionization chambers used in the testbeam detector

A schematic view of an ionization chamber is shown in figure 4.2 [Eng99]. The structure of the chamber is identical to the structure of the ionization chambers used in the top layer of the KASCADE-Grande calorimeter. It consists of a stainless-steel box with an

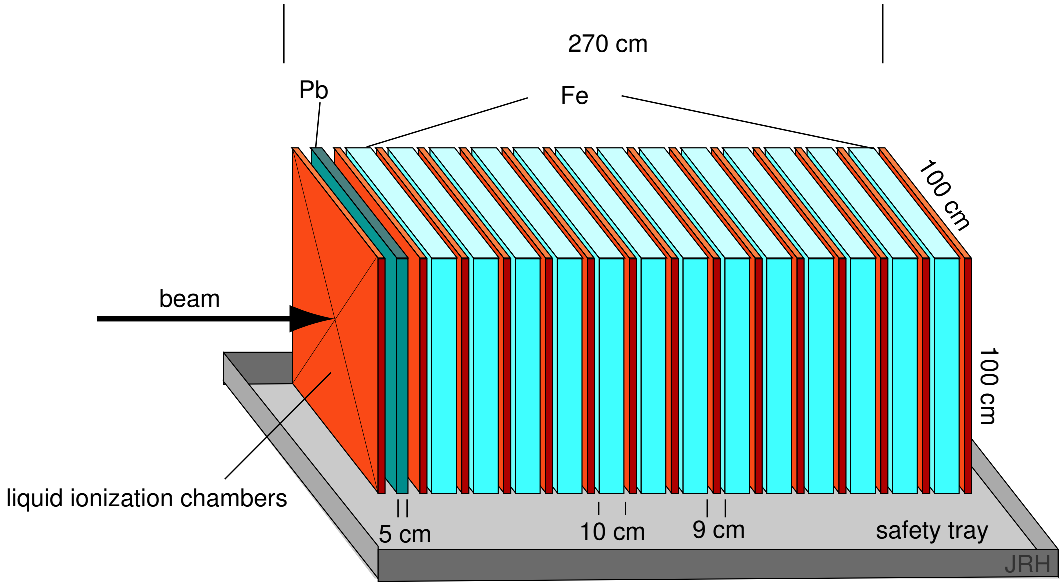

Figure 4.1: The setup of the testbeam detector [Hör04].

area of $50 \times 50\,\text{cm}^2$ and a thickness of 1.7 cm. The active material has a thickness equal to $2 \times 0.7\,\text{cm}$.

Each chamber is divided into four pads and each pad contains one electrode with an area of $25 \times 25\,\text{cm}^2$ and a thickness of 1 mm. The electrodes are placed in the middle plane of the box using ceramic spacers (Al_2O_3). A ceramic feed-through is used to pass the high voltage on the electrodes and to read out their signals. On top of the box there is a preamplifier housing containing four capacitors, one for each of the four pads. The preamplifier is placed directly on the box in order to avoid any parasitic capacitance of the connection cables (see also section 4.4).

Through a filling nozzle the chambers are filled with 1.75 l of the room temperature liquid tetramethylpentane (TMP, C_9H_{20}). The properties of TMP are given in table 4.1.

4.2.2 Liquid ionization chambers at room temperature

Liquids are preferred to gases, firstly because they have a higher density. A higher density leads to a larger number of ion-electron pairs generated, therefore more energy is deposited. In addition, the effect of diffusion of charged particles in liquids is smaller than in gases, so the track will be less broad.

The advantages of using liquid ionization chambers can be summarized as follows:

- the signal generated in liquid ionization chambers is proportional to the deposited energy,
- the response is characterized by spatial uniformity, i.e. it is independent on the position where the particle hits the chamber,
- liquid ionization chambers also ensure a large dynamic range, in the case of the KASCADE-Grande calorimeter it is approximately 0 to $5 \cdot 10^4$,

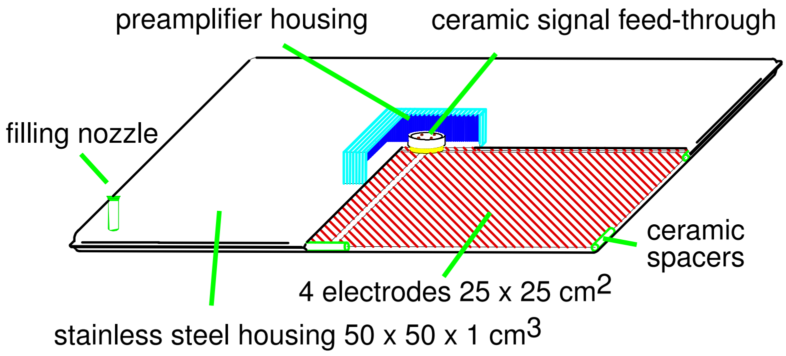

Figure 4.2: Schematic view of a liquid ionization chamber [Eng99].

- they provide long-term stability, due to the feed-back amplification.

Ionization chambers filled with liquid noble gases are widely used. In the 1960's it was found that room temperature liquids offer a high electron mobility [Eng96]. Studies showed that this high mobility is due to the spherical molecular structure.

Room temperature liquid ionization chambers were first used in the 1980's. The choice of TMP and TMS for the KASCADE-Grande calorimeter, from the high mobility room temperature liquids, was based on two criteria: high charge yield and low costs. TMS has been chosen because of its low price. The TMP has been taken from the UA1 upgrade calorimeter at CERN [Eng99]. Several properties of TMP and TMS are given in table 4.1.

	Tetramethylpentane (TMP)	Tetramethylsilane (TMS)
Dielectric constant ε_r ($T = 20°$ C)	1.98	1.92
Density ρ ($T = 20°$ C)	$0.7195\ \frac{\mathrm{g}}{\mathrm{cm}^3}$	$0.645\ \frac{\mathrm{g}}{\mathrm{cm}^3}$
Boiling temperature	122.7° C	26.5° C
Electron mobility	$(29 \pm 2)\,\frac{\mathrm{cm}^2}{\mathrm{Vs}}$	$(105 \pm 5)\,\frac{\mathrm{cm}^2}{\mathrm{Vs}}$
Charge yield per 100 eV G(0)	0.75 ± 0.05	0.61 ± 0.08

Table 4.1: Properties of the two room temperature liquids used to fill the liquid ionization chamber of the hadron calorimeter in the KASCADE-Grande experiment (TMP and TMS) [Eng96]. For the testbeam calorimeter only chambers filled with TMP have been used.

The main disadvantage of liquids is the presence of electronegative impurities, such as oxygen, which will reduce the number of drifting electrons due to attachment processes (see subsection 4.2.3). To limit this effect a high level of purification is needed. However, purification to a desired level can not be attained for any type of liquid. This is why only noble gases (e.g. xenon and argon) and a few hydrocarbons are used as media in liquid ionizing chambers. For room temperature liquids a purity level in the 1 ppb range is needed.

A detailed description of the purification process applied for the liquid ionization chambers used in the hadron calorimeter of the KASCADE-Grande experiment can be found in [Eng99].

4.2.3 Signal generation in an ionization chamber

An ionization chamber is like a parallel-plate capacitor filled with an active medium. When a charged particle passes through the active medium, ionization of the atoms in the material takes place. The number of ion-electron pairs created is given by:

$$N^0_{e^-} = \frac{E}{W} \ , \tag{4.1}$$

where E is the energy of the charged particle and
W is the mean ionization energy.

In the electric field, generated by the voltage applied to the plates, electrons will be accelerated towards the anode while ions drift towards the cathode. The acceleration is interrupted by collisions, therefore the maximum velocity particles can reach along the field lines is limited. The average velocity is the drift velocity. If we assume that the charged particles produced drift with a constant velocity, the maximum drift time of the electrons between the plates of the capacitor is given by:

$$t_d = \frac{d^2}{\mu_{e^-} \cdot U} \ , \tag{4.2}$$

where d is the distance between the plates of the capacitor,
μ_{e^-} is the electron mobility and
U is the applied voltage.

For the ionization chambers used here, with TMP as active medium, the drift time is $1\,\mu$s.

The response of an ionization chamber is given by the number of ion-electron pairs, which are collected at the electrons. Not all ion-electron pairs are collected due to three main processes: primary recombination, signal damping and electron attachment.

- *Primary recombination*: For minimum ionizing particles the distance between two consecutive ionization processes along the track is large compared to the thermalization length. Therefore the electron sees only the electric field of the mother ion and recombination will take place. Due to the electric field and the thermal atomic movement a part of the electrons will escape the primary recombination. The charge yield gives the number of these electrons, conventionally for an energy deposited of $E = 100\,\mathrm{eV}$. The relation between the electron yield $G(E)$ and E can be parameterized for TMP as [Hör94]:

$$G_{TMP}(E) = 0.678 + 5.30 \cdot 10^2 \frac{E}{\mathrm{kV/\,cm}} - 8.19 \cdot 10^{-4} \left(\frac{E}{\mathrm{kV/\,cm}} \right)^2 . \tag{4.3}$$

- *Signal damping*: In a hadron calorimeter an important part of the signal generated in the cascade is due to strongly-ionizing particles. In the case of strongly-ionizing particles, the distance between the ions is in the same order as the thermalization length. This means the electron is influenced not only by the mother ion but also by other ions. Therefore, the probability of recombination will increase. This probability of recombination is called the damping factor $D(\alpha)$. It depends on the angle α between the ionization track and the electric field.

- *Electron attachment*: The electron life time τ in medium is very important. In order to collect as much as possible of the total charge produced (neglecting primary recombination and signal damping), τ should be much larger than the electron drift time t_d. The life time is limited by the presence of electronegative impurities in the liquid (e.g. O_2, H_2O, CO_2), since free electrons are captured by the electronegative atoms, before they are collected. The resulting negative ions are slowly moving and therefore will lead to a reduction of the fast signal. The number of collected charge carriers is given by:

$$f(t_d, \tau) = \frac{\tau}{t_d}\left(1 - \frac{\tau}{t_d}\left(1 - e^{-\frac{t_d}{\tau}}\right)\right). \tag{4.4}$$

Taking into account all these effects, that influence the number of collected free charge carriers, the detectable charge is given by:

$$Q = 2\ d\ \frac{dE}{dx} \cdot \frac{G(E)}{100\,\mathrm{eV}} \cdot f(t_d, \tau) \cdot D(\alpha). \tag{4.5}$$

It depends on the energy loss $\frac{dE}{dx}$, the charge yield $G(E)$, the damping factor $D(\alpha)$ and on the number of collected charge carriers $f(t_d, \tau)$.

4.3 Data taken

The calorimeter was set up and tested at the H4 beamline of the Super Proton Synchrotron (SPS) at CERN. The test took place in 2003 during two periods. The first period lasted from the 8^{th} until the 18^{th} of June and the second period from the 8^{th} until the 16^{th} of July.

During the first period the setup used was exactly the one described in section 4.1. In the second test period, a lead plate with a thickness of 15 mm, corresponding to three interaction lengths, was placed in front of the first layer of liquid ionization chambers. This was done in order to identify electrons. The signal of the ionization chambers in the first layer has been used to select primary electrons.

For trigger purposes two plastic scintillators were used in coincidence in front of the calorimeter. Additionally, in order to be able to identify muons, a third scintillator was placed behind the calorimeter.

Each layer of liquid ionization chambers consists of 4 chambers, and as mentioned in subsection 4.2.1, each chamber has 4 pads. A layer is divided into 16 pads as shown in figure 4.3, corresponding to 16 electronic channels.

All data were taken with the beam hitting a fixed spot in one of the pads, 4 cm to the left and 4 cm below the center of the calorimeter. This pad will be called the *hit* pad, and the inner four pads will be called *central* pads. The reason for the beam spot

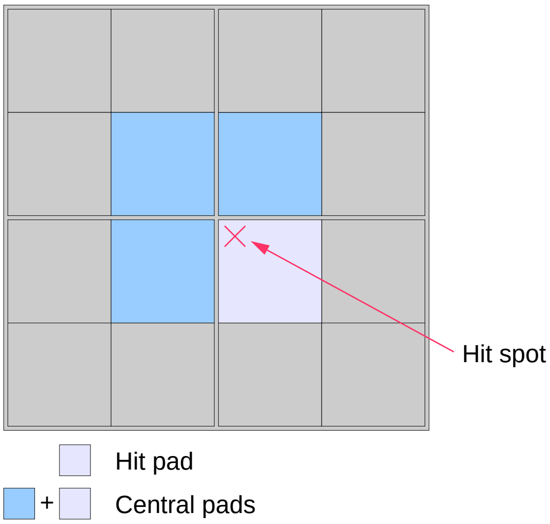

Figure 4.3: Structure of a layer in the testbeam calorimeter.

being fixed for the entire testbeam period is that neither the calorimeter nor the beam could be moved.

Data were taken for three types of particles (muons, electrons and hadrons), with energies between 15 GeV and 350 GeV and at three different voltages (5000 V, 4500 V and 4000 V). Protons and pions could not be distinguished, they were treated as hadrons (π/p). However, during the analysis they will be referred to as pions. In between the spills, random events were also recorded. These events will be used to determine the value of the pedestal.

After looking into the logbook, some of the runs were eliminated due to several reasons, namely: test runs, unstable data, run stopped due to low number of particles, electronics problems during the run, beam tuned by the operator during the run or wrong input (wrong particle type or wrong energy). The remaining runs are considered good.

Table 4.2 gives a summary of the good runs for the two test periods, at a high voltage setting of 5000 V (only a few runs were taken at other voltage settings).

A complete list of the data taken can be found in appendix A. In between the runs electronics calibration data were taken.

4.4 Calibration of the read-out electronics

The usage of liquid ionization chambers ensures a high dynamic range. This is especially necessary in air shower experiments, where both the energy deposited by a minimum ionizing particle and the energy deposited by a high energy hadron have to be measured.

The read-out electronics of the testbeam calorimeter is identical to the one used in the calorimeter of the KASCADE-Grande experiment. As shown in figure 4.4 the feedback amplifier chain consists of a preamplifier placed directly on the ionization chamber and a main amplifier. Twisted pair cables are used to connect them. The detector signal reaches the preamplifier through a coupling capacitor C_K which is composed of three

Period	Particle type	Energy [GeV]	No. of good runs	Total number of events
1^{st} period	π/p	15	2	43 672
		30	1	85 909
		50	1	112 421
		100	2	195 600
		150	2	217 234
		200	3	272 105
		250	1	112 400
		300	1	112000
	μ	150	3	110 418
	e^-	30	1	148 548
		50	1	119 469
		150	1	113 556
		200	1	112 714
		250	1	110 462
2^{nd} period	π/p	15	2	94 656
		30	2	121 187
		50	2	235 119
		100	2	231 257
		150	1	111 998
		200	1	110 616
		250	1	115 553
		300	1	110 135
		350	1	113 340
	μ	50	1	112 430
		100	1	148 840
		200	1	132 287
		250	1	187 890
	e^-	30	1	133 640
		50	1	115 068
		100	1	130 943

Table 4.2: List of the good runs. For the two test periods the number of good runs and the total number of events are given for each type of particle at different energies.

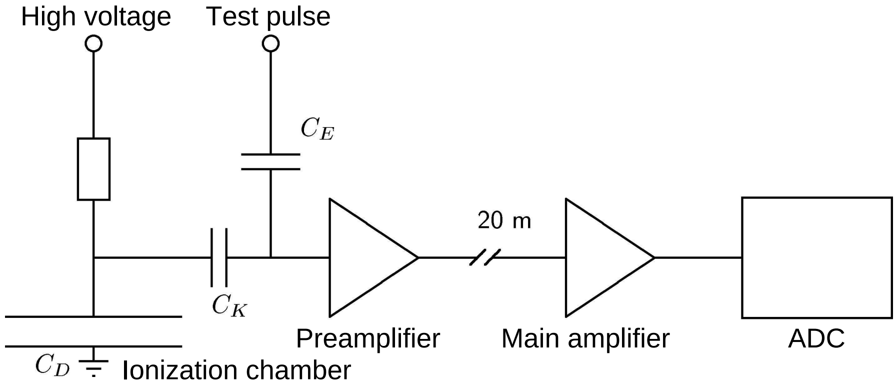

Figure 4.4: Electronic chain (modified from [Hör94]).

ceramic capacitors of 3.3 pF each. The total capacity is equal to 9.9 pF. The coupling capacitor collects the charge from the detector and then is read by the preamplifier.

For the calibration of the electronic chain, test pulses are applied to a precision capacitor C_E. Signals from the detector have also been measured. Although the same charge was applied in both cases, the signals measured after the preamplifier differ. Therefore a correction factor K equal to:

$$K = 1 + \frac{C_D}{C_K} \tag{4.6}$$

is applied.

This factor accounts for the difference between the amplitude,that the preamplifier sees due to a signal coming from the detector, and the amplitude, it sees when test pulses are applied. The derivation of this correction factor can be found in [Hör94].

An additional correction has to be applied to account for the dependence of the capacitance of the coupling capacitor on the high voltage applied to the chamber. The voltage dependence can be parameterized by [Hör94]:

$$C_K(U) = \left[1.00 - 2.43 \cdot 10^{-2} \frac{1}{\mathrm{kV}} U - 2.19 \cdot 10^{-2} \frac{1}{\mathrm{kV}^2} U^2\right] \cdot 3.3\,\mathrm{pF}. \tag{4.7}$$

In order to effectively use the large dynamic range, that the liquid ionization chambers ensure, a nonlinear characteristic curve has been chosen for the amplifier and digitization chain.

As seen in figure 4.5, the curve has a linear part in the range of low ADC values, followed by an exponential part and for very high ADC values (above 7000 ADC counts) by a parabola.

The curve is parameterized by a 12-parameter formula [Ruh96].

$$Q(x) = \delta_1 Q_1 + \delta_2 \delta_3 Q_2 + \delta_4 Q_3 \tag{4.8}$$

$$\begin{aligned}
\text{with:}\quad & Q_1(x) = p_1(x - p_0) + p_2(x - p_0)^2, && \delta_{1/2} = \tfrac{1}{2}\left(1 \mp \tanh\left(\tfrac{x-u_1}{100}\right)\right),\\
& Q_2(x) = e_0 + e_1 x + e_2 \log(e_3 - x), && \delta_{3/4} = \tfrac{1}{2}\left(1 \mp \tanh\left(\tfrac{x-u_2}{10}\right)\right),\\
& Q_3(x) = q_0 + q_1 x + q_2 x^2.
\end{aligned}$$

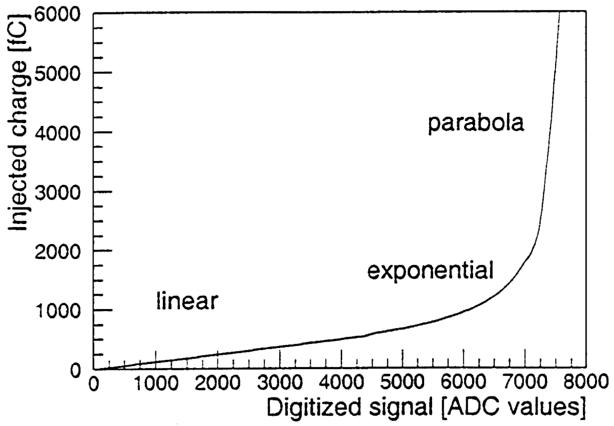

Figure 4.5: Signal characteristic of the amplification and digitization chain [Eng99].

The p_0 parameter is an estimate of the electronics pedestal and will be used through out the analysis for the pedestal correction of the ADC counts.

For most of the data taken during the testbeam, the ADC counts recorded correspond to the linear part of the curve. However, at energies higher than 100 GeV events outside the linear part were also recorded. The largest number of such events has been recorded for 350 GeV pion runs, around 10% of the total number of recorded events. During the analysis no special correction has been applied for these events. However, this is a source of systematic errors. The effect of these events on the final result will be discussed in section 5.5.

The entire electronic chain provides a dynamic range of $\sim 6 \cdot 10^4$ corresponding to a measured charge from 0.1 fC to 6000 fC [Hör94].

Chapter 5

Data analysis

The aim of the analysis is to determine the performance of the testbeam calorimeter. First the pedestal value is obtained and its stability with time is verified. Then the calibration of the central pads is performed. Applying the calibration, longitudinal energy distribution curves are obtained. The final result of the analysis is the energy resolution of the calorimeter. Several systematic studies are also presented.

All results have been obtained using data runs from the second test beam period only. During the first period commissioning and engineering runs have been performed. Besides the data taken during the test beam, data obtained using Monte Carlo simulations employing the GEANT[GEA93]/FLUKA[Mil00] code, have been used.

5.1 Pedestal determination and stability

The first step in the analysis is to determine the pedestal value and its stability within the time interval between the start and the end of each run.

For each run spills of real events have been recorded. These are events where particles hit the calorimeter. In between the spills also random events have been recorded. These are events recorded with no activity in the detector. Therefore, the ADC counts obtained for these events are a measure of the electronics pedestal. For the analysis, the pedestal subtracted ADC counts have to be used. This means that on an event by event base, the pedestal value has to be subtracted from the ADC value. In order to find the pedestal value, the random events have been used. During each period in between two spills a set of 100 events has been recorded. One histogram is filled for each set. Then the pedestal distribution obtained is fitted using a Gaussian function. The resulting mean parameter of the fit gives the mean value of the pedestal for the corresponding spill.

The values obtained differ from spill to spill. If the fluctuation of the pedestal mean value from spill to spill is larger than one sigma of the pedestal distribution, a pedestal correction spill by spill has to be applied. Otherwise a common value can be used for the entire run.

In other words, the pedestal stability with time has to be checked. For this check the pedestal mean value (p_i) vs. the spill number is plotted (see figure 5.1, upper plot). The errors on the points are the errors of the mean parameter obtained from the fit. As the plot shows, the pedestal values fluctuate less than 10% around the mean value. For the example shown, the mean value is equal to 54.28 ADC counts.

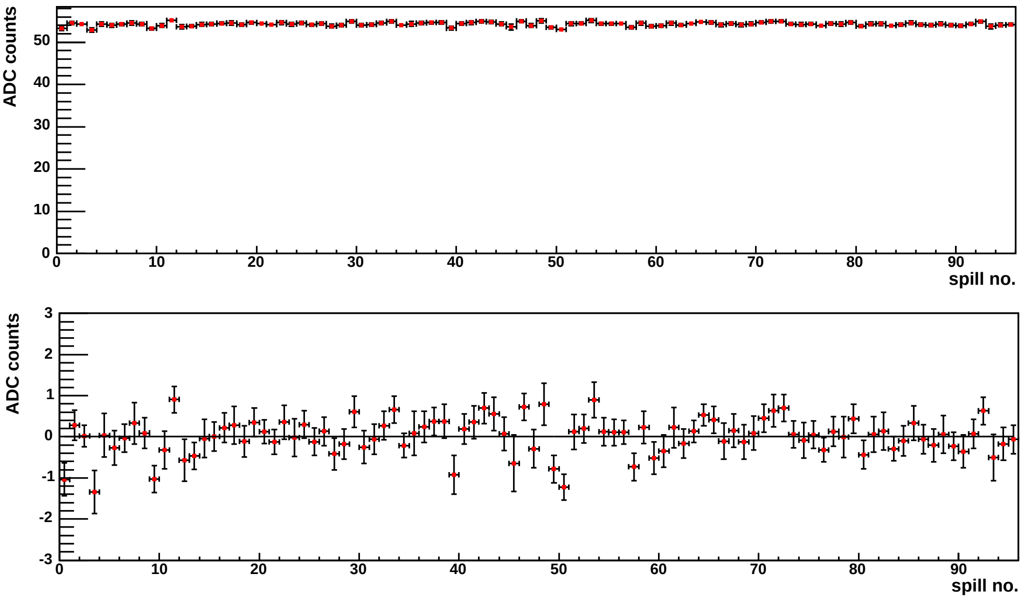

Figure 5.1: Check of the pedestal stability with time. The upper plot shows the pedestal mean value (p_i) vs. spill number. The lower plot shows the difference between p_i and the weighed average Av vs. spill number. These plots have been obtained for the hit pad in layer three, using data from Run 115.

In order to verify if there is any kind of structure in these fluctuations, the difference d_i between p_i and the weighted average Av (see figure 5.1 lower plot) is also plotted. The weighted average, i.e. the average weighted by the errors, is computed over all spills according to the following formula:

$$Av = \frac{\sum_i^N \frac{p_i}{(\Delta p_i)^2}}{\sum_i^N \frac{1}{(\Delta p_i)^2}}, \tag{5.1}$$

where N is the number of spills.

In order to obtain the error (Δd_i) on the difference ($d_i = p_i - A_v$), error propagation is used. Taking into account the correlation between the error of the pedestal mean for a spill and the error on the weighted average, Δd_i is calculated according to:

$$(\Delta d_i)^2 = (\Delta p_i)^2 - (\Delta Av)^2 \ , \tag{5.2}$$

where the error on the weighted average is given by:

$$(\Delta Av)^2 = \frac{1}{\sum_i^N \frac{1}{(\Delta p_i)^2}} \ . \tag{5.3}$$

Figure 5.1 shows a random fluctuation of the pedestal mean values with a maximum deviation from the weighted average of less than two channels. To determine the mean fluctuation a projection on the y axis of the plotted values is performed (see figure 5.2). The result is a Gaussian distribution with a mean of ~ 0.06 ADC counts and a sigma of 0.36 ADC counts. Hence, the pedestal mean value for one spill has a fluctuation of less

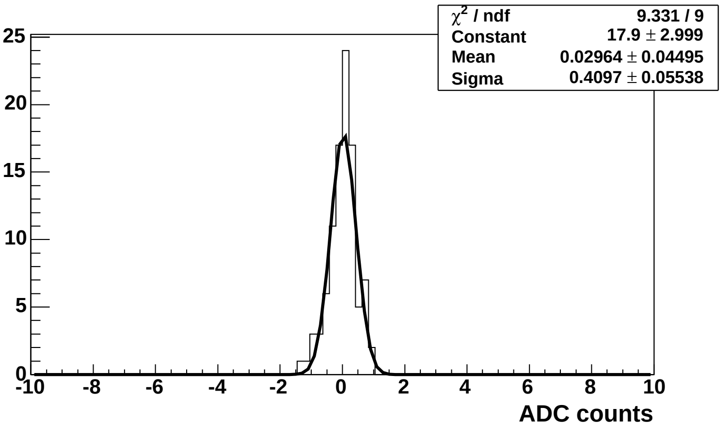

Figure 5.2: Distribution of the fluctuations of the pedestal mean p_i around the weighted average Av.

than 12% of one sigma of the pedestal distribution (3.22 ADC counts). Thus, there is no need to apply the pedestal subtraction spill by spill, and a global value can be used for the entire run for each channel.

The plots shown have been produced for the hit pad in layer three and all the numbers given have been obtained for this example. The same checks have been done for all runs and for all channels and no significantly different behavior has been noticed.

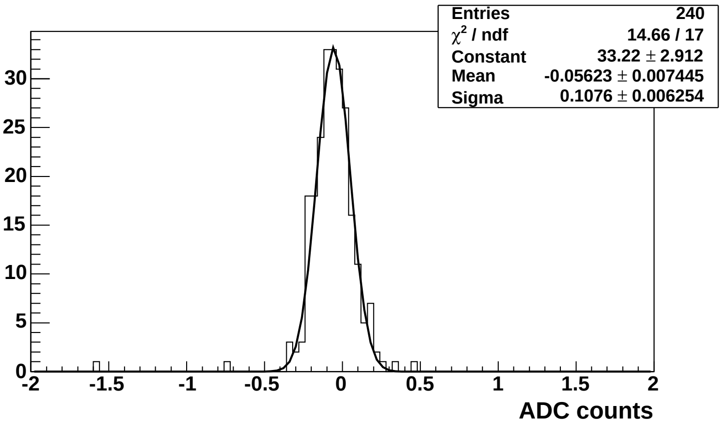

Figure 5.3: Distribution of the difference between the pedestal value determined using the random events taken in between the spills and the value of the pedestal obtained from the electronic calibration data.

As the global value for the pedestal the value obtained from the electronic calibration has been used. More precisely, the p_0 parameter of the function 4.8, which describes the characteristic curve of the electronic chain (see chapter 4, section 4.3) is used as an estimate for the pedestal value. The electronic calibration has been performed in between the runs, and for each channel the set of parameters has been determined. To justify the use of the p_0 parameter, the difference between the pedestal value determined using the random events taken in between the spills and the value of the p_0 parameter is computed for each channel (15 layers × 16 pads). The distribution obtained is shown in figure 5.3 and it has a sigma significantly smaller than one sigma of the pedestal distribution. More important, the mean of the distribution, thus the bias introduced by using p_0, is only 13% of the sigma of the pedestal distribution. Therefore the use of the p_0 parameter is justified.

To conclude, the study showed, that the pedestal is stable during one run within less than one sigma of the pedestal distribution. Hence, no spill by spill correction is needed and the pedestal correction within one run will be done by using a single global constant for each channel. The global constant is obtained from the electronic calibration. The difference between the value of the global constant p_0 and the mean value of the pedestal distribution for a certain pad is a source of systematic errors. The effect of this difference on the final result will be disscused in section 5.5.

5.2 Calibration of the hit pad using muon data

The second step of the analysis is the muon calibration. Normally, the muon calibration has to be done for each pad. However, all data have been taken with the beam hitting just the hit pad. Hence, the muon calibration can only be applied for this pad. A set of 15 muon calibration constants is obtained, one constant for each of the 15 active layers of the calorimeter ($C_{\mu,layer}$). They give the relation between the energy units (GeV) and ADC counts.

The calibration constants are obtained for data of 100 GeV muons. However, the energy deposited by a muon changes only minimally with the energy of the particle, according to the Bethe-Bloch formula. Hence, the same calibration constants obtained for 100 GeV muon data can also be used for data at different energies.

5.2.1 Procedure

In order to obtain the calibration constants, besides the muon data taken during the testbeam, also data obtained using a Monte Carlo (MC) simulation are used, both at an energy of 100 GeV.

Monte Carlo simulation data

Using the MC data, histograms are filled with the energy deposited in the hit pad for each of the 15 layers. A high energy muon (100 GeV and even higher) will lose energy through ionization and δ-rays as explained in chapter 3. The energy loss due to these mechanisms is typically 1 to 2 $\mathrm{MeV g^{-1} cm^{2}}$. According to the Bethe-Bloch formula, the mean energy deposited by a muon in 1 cm of material equals 95.5 MeV for iron, 50.8 MeV for lead and 1.9 MeV for TMP. This means that a 100 GeV muon will go through the testbeam calorimeter without being absorbed. The amount of energy deposited will on average be the same in each layer. Figure 5.4 shows the typical shape of the energy distribution.

It has a Landau shape with a most probable value (mpv) around 2 MeV and a long tail up to energies of several GeV or more. For the determination of the calibration constants a cut is applied for events with an energy deposited greater than 100 MeV. These are events, in which energetic charged particles result from the muon interaction with the absorber material. These particles deposit energies up to several GeV. These

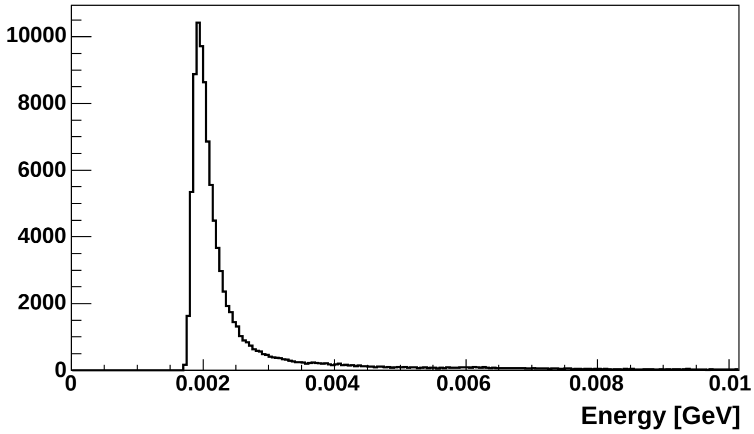

Figure 5.4: Distribution of the energy deposited by a 100 GeV muon, for the hit pad in layer five. MC simulation data have been used.

events are excluded by a cut, since they distort the measurement of the energy deposited by a muon. The number of events excluded is $\sim 0.2\%$ of the total number of events.

Using the distributions obtained after the cut, the mean values of the entries are taken, for all 15 layers. This gives the values of the mean energies deposited ($m_{MC,layer}$), in the hit pad of each single layer.

Measured data

During the second testbeam period only one muon run has been taken for each energy. Therefore, the 100 GeV muon run is splitted into two. The first half is used to determine the calibration constants and the second to check them.

Like for the MC simulation data, a histogram is filled for each of the layers (see figure 5.5). First, using the random events taken in between the spills the pedestal distribution is plotted. Second, using the events in the spills the signal distribution is plotted.

The signal distribution has two peaks:

- the first peak corresponds to the noise events in the signal,
- the second peak corresponds to the real signal.

In both cases the pedestal subtracted ADC counts are used.

For the signal distribution two cuts are introduced.

- One cut is made on the events with zero ADC counts. The reason for recording events with absolute zero ADC counts is not well understood. The most likely is a malfunctioning of the electronic chain, therefore they are excluded from the analysis. If one channel reads out zero ADC counts before pedestal correction, than the entire event is excluded. With this cut 40% of the events have been excluded.
- The second cut corresponds to the cut done for the MC simulation data on the events with energies deposited greater than 100 MeV. In this way both measured and simulated data are treated in the same way.

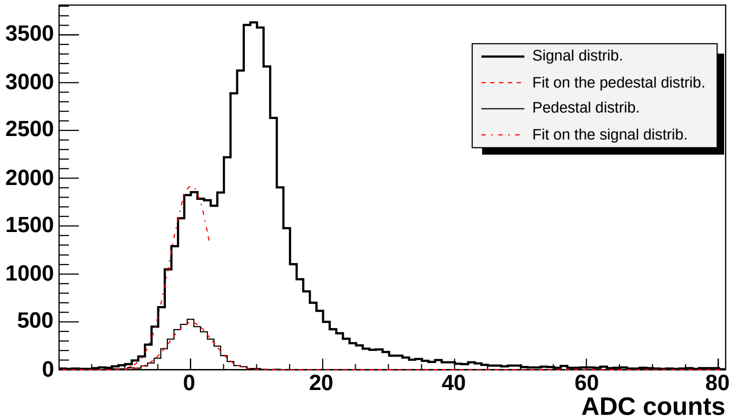

Figure 5.5: Pedestal and signal distributions obtained for the hit pad, layer five (zoom on the x axis). 100 GeV muon data from Run 125 have been used.

A different set of calibration constants has been obtained before, using a different procedure. To obtain the cut in ADC counts corresponding to the 100 MeV cut in energy, these 'old' calibration constants are used (${}^{old}\mathrm{C}_{\mu,layer}$). The following procedure has been used to obtain the 'old' calibration constants.

- For the MC data the same distribution as in figure 5.4 is plotted. However, no cut is done and the distribution is fitted using a Landau function. Instead of taking the mean of the histogram the most probable value (mpv_{MC}) of the Landau fit function is used to obtain the calibration constants.

- Using the measured data the same distribution as in figure 5.5 is plotted. A Gaussian function is used to fit the pedestal distribution. The resulting mean (m_{ped}) and sigma (σ_{ped}) parameters are then used to describe the noise contribution to the signal. In order to exclude the noise events a Gaussian plus Landau shape is used to fit the signal distribution. For the Gaussian part of the fit function, which describes the noise, the mean and sigma parameters are fixed to the values obtained from the pedestal distribution: m_{ped} and σ_{ped}. The Landau part of the fit function describes the real signal. Just like for the MC the value used to obtain the calibration constants is the most probable value (mpv_{data}) of the Landau function.

- Having determined mpv_{MC} and mpv_{data} the 'old' calibration constants are given by the ratio:

$$ {}^{old}\mathrm{C}_{\mu,layer} = \frac{mpv_{MC}}{mpv_{data}}. \tag{5.4}$$

This procedure works for the muon data. However, the Gaussian plus Landau shape does not describe the pion[1] distribution well. One possible explanation is the muon contamination of the pion data. Some of the pions in the beam decay into muons before reaching the calorimeter. This gives rise to a third peak in the signal distribution.

The method can be improved by finding a function that describes both the muon and the pion distribution. Additional studies, where a similar muon contribution is added

---

[1] During the test beam, pions and protons could not be distinguished. They are referred to as pions.

to the MC simulation, are needed. For this analysis a more straightforward method has been chosen: a statistical subtraction of the noise events. The method will be described in detail later in this section. For consistency, the latter is used for muons also.

Returning to the method used in this analysis, the cuts in ADC counts (cut_{ADC}) corresponding to the 100 MeV cut in energy (cut_{energy}) are obtained using the ratio:

$$cut_{ADC,layer} = \frac{cut_{energy}}{{}^{old}\mathrm{C}_{\mu,layer}}. \tag{5.5}$$

Thus, different cuts are applied for different layers.

In order to obtain the muon calibration constants the mean of the real signal, is needed, this means without the noise contribution, like in the MC simulation. This is achieved by statistically subtracting the noise events.

- First, like in the previous method, the pedestal distribution is fitted using a Gaussian function (see figure 5.5). The mean (m_{ped}) and sigma (σ_{ped}) parameters obtained from the fit are used in the next step.

- Second, unlike in the previous method, where the entire signal distribution is fitted, only the first peak of the distribution, which describes the noise contribution is fitted. For the fit a Gaussian function is used. The mean parameter is fixed to the m_{ped} value and the sigma parameter to the σ_{ped} value. This means, that the only free parameter is the amplitude. The range, within which the distribution is fitted, is also fixed. The range differs for each layer. In order to choose it, each histogram is visually inspected. The value of the amplitude parameter resulting from the fit, divided by the width of the bin of the histogram, gives the number of noise events in the signal.

  The number of noise events (N_{noise}) is known. Multiplied by the mean of the pedestal distribution (m_{ped}), it gives the noise contribution to the global signal. The total number of events N_{GS} is also known. N_{GS} multiplied by the global mean m_{GS} gives the global signal. In order to determine the real signal $m_{data,layer}$, the noise contribution is subtracted from the signal distribution. Hence, the mean of the real signal is given by:

$$m_{data,layer} = \frac{N_{GS} m_{GS} - N_{noise} m_{ped}}{N_{GS} - N_{noise}}. \tag{5.6}$$

$m_{data,layer}$ is taken as a function of three uncorrelated variables N_{noise}, m_{GS} and N_{noise} (N_{GS} is constant) and the error on $m_{data,layer}$ is calculated according to:

$$\left(\sigma_{m_{data,layer}}\right)^2 = \left(\frac{\partial m_{data,layer}}{\partial m_{GS}}\right)^2 \sigma^2_{m_{GS}} + \left(\frac{\partial m_{data,layer}}{\partial N_{noise}}\right)^2 \sigma^2_{N_{noise}} + \left(\frac{\partial m_{data,layer}}{\partial m_{ped}}\right)^2 \sigma^2_{m_{ped}}. \tag{5.7}$$

The partial derivatives are calculated and the following formula is obtained for the error:

$$\left(\sigma_{m_{data,layer}}\right)^2 = \left(\frac{N_{GS}}{N_{GS} - N_{noise}}\right)^2 \sigma^2_{m_{GS}} + \left(\frac{N_{GS}(m_{GS} - m_{ped})}{(N_{GS} - N_{noise})^2}\right)^2 \sigma^2_{N_{noise}} + \left(\frac{N_{noise}}{N_{GS} - N_{noise}}\right)^2 \sigma^2_{m_{ped}}. \tag{5.8}$$

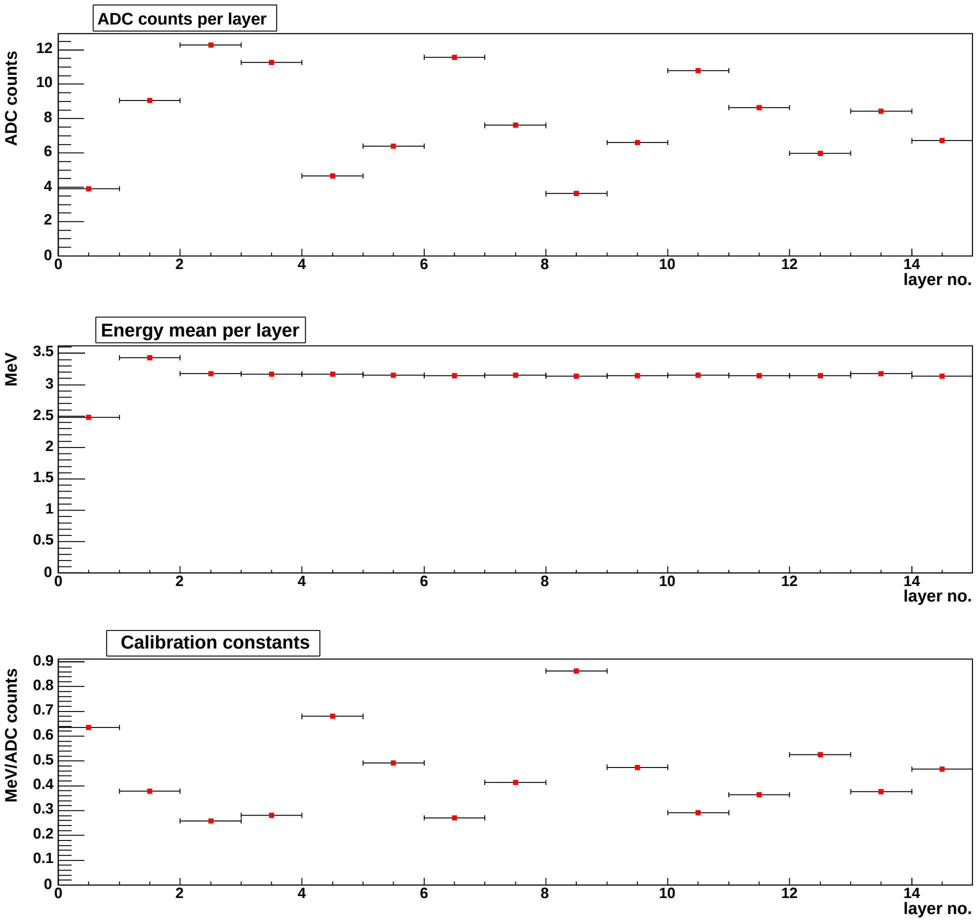

Figure 5.6: Derivation of the calibration constants using the first half of Run 26.

5.2.2 Results

The procedure explained above is used for all 15 layers. The upper plot in figure 5.6 shows the mean ADC counts vs. layer number. The number of ADC counts corresponding to the energy deposited varies from layer to layer. These variations are due to differences in efficiencies and life times between the chambers.

The middle plot in figure 5.6 shows the mean energy deposited vs. the layer number. As mentioned before, one would expect a muon to deposit roughly the same amount of energy in each of the 15 layers. However, there is a significant difference between the energy deposited in the first two layers compared to the energy deposited in the other layers. The energy deposited increases from $\sim 2.5\,\mathrm{MeV}$ in the first layer to $\sim 3.5\,\mathrm{MeV}$ in the second layer and then decreases to an average of $\sim 3.15\,\mathrm{MeV}$ for all the other layers. This variation is explained by the difference in the structure of the calorimeter in the first 2 layers compared to the other layers. In front of the first layer of liquid ionization chambers there is a 15 mm layer of lead absorber. Between the first and second active layer a thicker (5 cm) lead layer is placed. The δ-rays which result from the muon interaction with the lead absorber lead to an increase in the energy deposited by 40% between the second and the third layer. Starting behind the second layer of liquid ionization chambers, the calorimeter structure becomes regular. There is one layer of iron absorber between each two consecutive active layers. Hence, the energy deposited in these 13 layers shows only small variations in a range of 3.13 MeV to 3.18 MeV.

Having obtained for each of the 15 layers the mean energy deposited from the MC data and the mean number of ADC counts from the measured data, the muon calibration constants for the hit pad are determined by the ratio:

$$C_{\mu,layer} = \frac{m_{MC,layer}}{m_{Data,layer}} \ . \tag{5.9}$$

The lower plot in figure 5.6 shows the muon calibration constants. They differ from layer to layer and they compensate for:

- different efficiencies of the chambers,
- different electron life times in the TMP,
- different properties of the absorber material in front of each layer.

The same structure as used in the experiment is implemented also in the MC. In the MC simulation the iron layers are identical. In the experiment this is not true, since the properties of the material may differ from layer to layer. The calibration constants will compensate for these differences.

5.2.3 Check of the muon calibration constants

The calibration constants have been obtained using the first half of a muon data run (100 GeV muons). The second part of the run is used to check the stability of the calibration constants. Following the same procedure as explained before, the measured data are used to plot the pedestal and signal distribution. The noise contribution is statistically subtracted and the mean of the real signal ($m_{data,layer}$) is obtained, for each layer (see figure 5.7 upper plot). The energy reconstructed $E_{rec,layer}$ is obtained by multiplying $m_{data,layer}$ with the corresponding calibration constant:

$$E_{rec,layer} = C_{\mu,layer} \cdot m_{Data,layer}. \tag{5.10}$$

The middle plot in figure 5.7 shows a comparison between the energy deposited obtained from the MC simulation and the energy reconstructed from the measured data. The lower plot in figure 5.7 shows for each layer the difference between the energy obtained from measured and simulated data:

$$D = E_{data} - E_{MC}. \tag{5.11}$$

The errors on the points are computed using error propagation. For all layers the difference between data and MC is well within the errors.

In conclusion, applying a statistical subtraction of the noise contribution to the signal, the muon calibration of the hit pad has been performed. The energy reconstructed using the obtained calibration constants, agrees well with the energy obtained from the MC. This proves that the muon calibration works. The statistical subtraction of the noise is a source for a systematic error. The error it may introduce on the final result will be discussed in section 5.5.

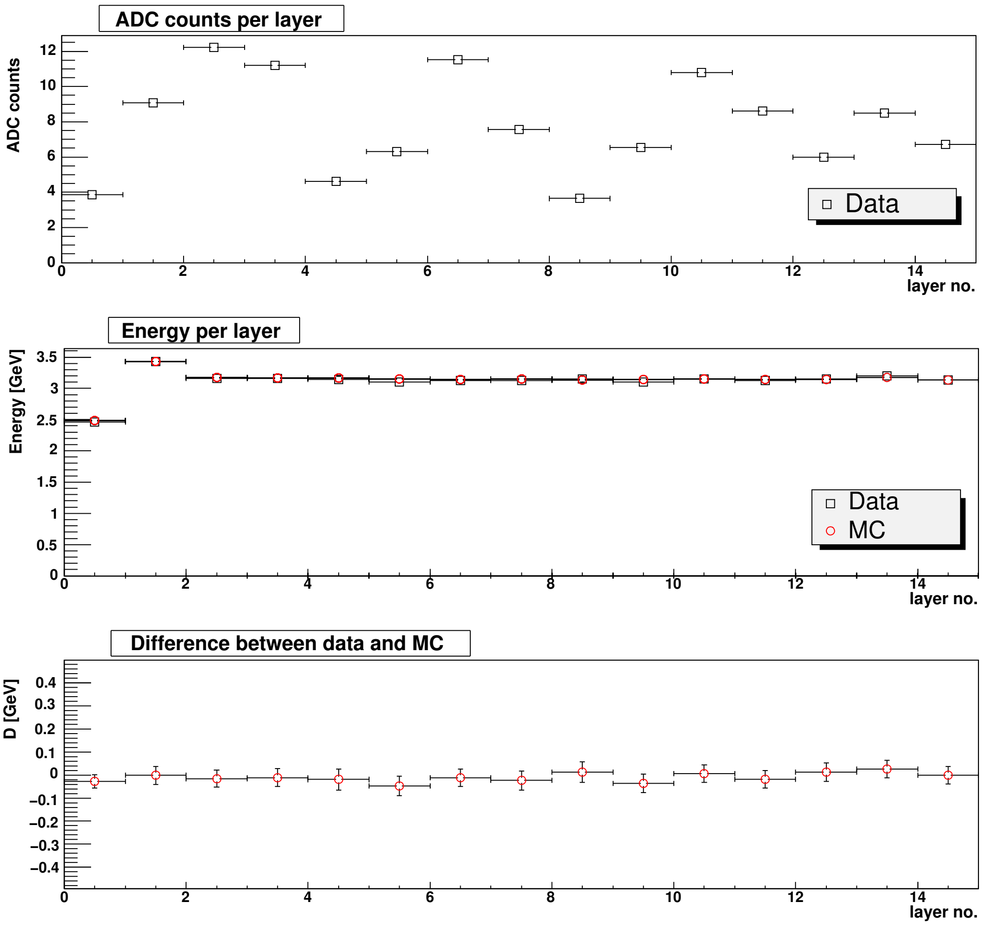

Figure 5.7: Check of the calibration constants for the second half of Run26.

5.3 Calibration of the central pads using pion data

The muon data have been analyzed and the energy calibration of the hit pad has been obtained using muon data. The next step in the analysis is to obtain the energy calibration of the other central pads, using pion data.

Two global cuts are done: one on the showers and one on the pads included in the analysis. The same cuts are done for both measured and simulated data.

Showers included in the analysis

The first cut is done on the starting layer of the shower. The amount of energy deposited in a certain pad strongly depends on the starting layer of the shower. Studies using MC simulations show, that for the same energy of the particle, the shower can start in any of the layers. For the analysis only showers starting in the second layer are considered. An example in shown in figure 5.8.

In appendix B two other examples are shown: one with a shower starting after layer seven and one with a shower stopping before layer seven.

In order to choose these events, cuts on the energy deposited in the first two layers are applied. To determine the value of the energy cut, 300 shower events from MC

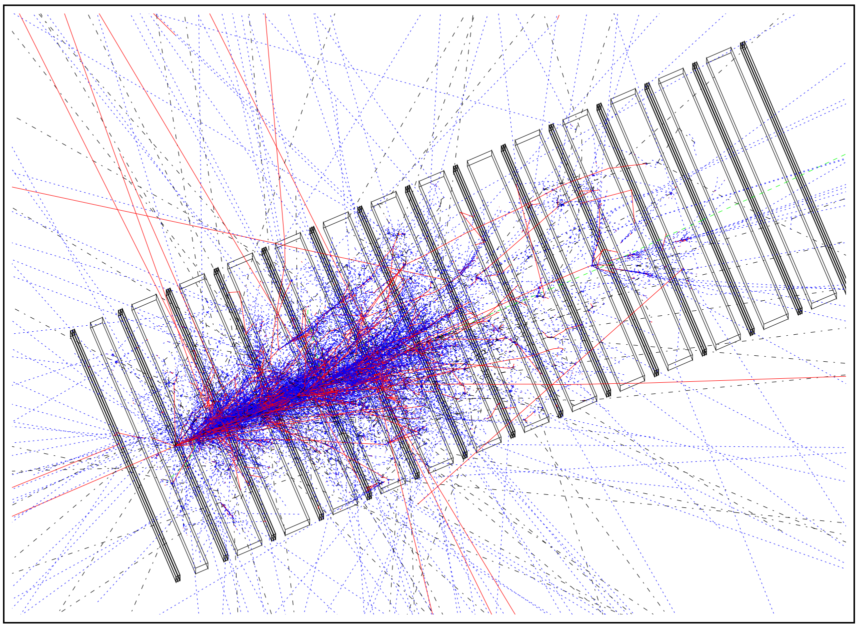

Figure 5.8: Display of an event starting in the second layer (MC). Color coding: red - charged particles, green - muons, blue - gammas and black - neutral particles or neutrinos.

simulations were visually inspected. Two histograms were filled:

- one with the energy deposited in the last layer outside the shower, for the example shown in figure 5.8 that is the energy deposited in the first layer,
- and one with the energy deposited in the first layer inside the shower, e.g. layer two in figure 5.8.

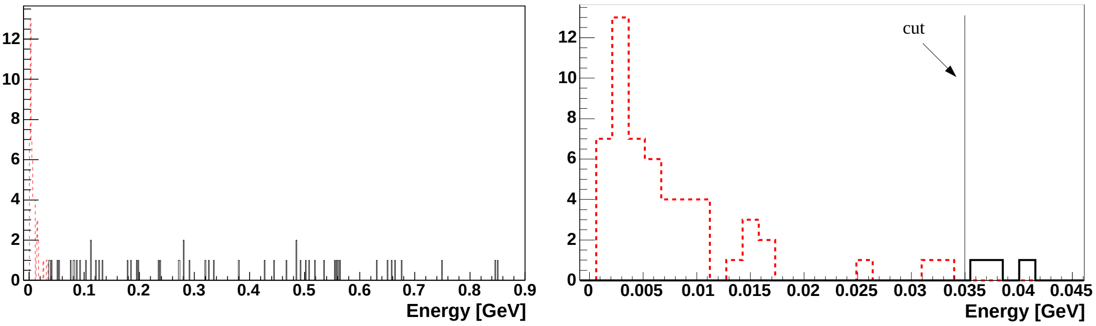

Figure 5.9: Determination of the energy cut applied in order to select events where showers start in the second layer. The left plot shows two histograms, with the energy deposited in the last layer outside the shower (red, dashed line) and in the first layer inside the shower (black, full line). The right plot is a zoom on the x axis. 150 GeV pion MC data have been used.

The two histograms are shown in the left plot in figure 5.9. In the right plot a zoom on the the x axis is applied to better visualize the gap between the histograms. The gap is at about 0.35 GeV, and gives the value of the energy cut. Hence, one cut is applied on the energy deposited in the first layer, which should be smaller than 0.35 GeV and another cut is applied on the energy deposited in the second layer, which should be larger than 0.35 GeV.

Pads included in the analysis

A decision on which pads to include in the analysis has to be taken. All data have been taken with the beam hitting only the hit pad. Thus, only the muon calibration of the hit pad was possible. For the pion calibration of the other pads a different method has to be applied.

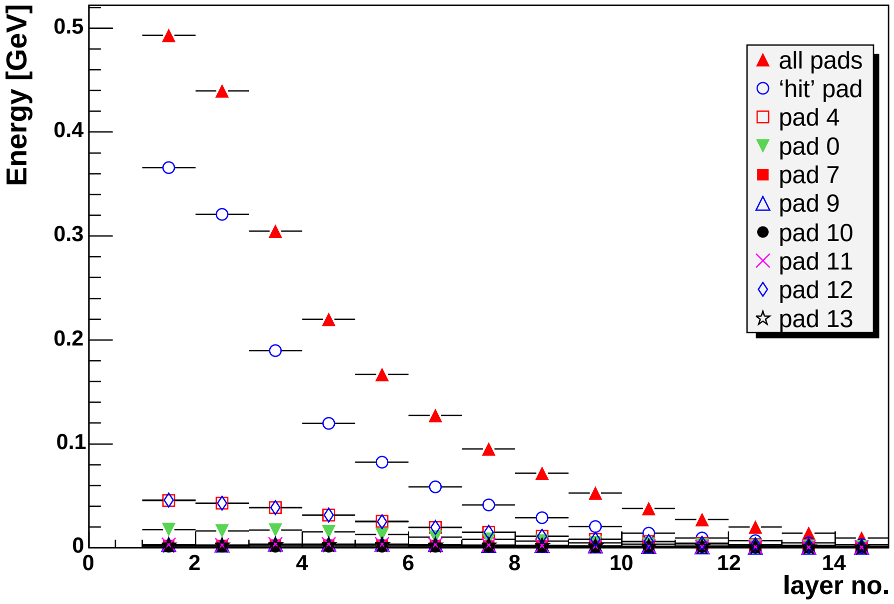

Figure 5.10: Longitudinal energy distributions for all pads, obtained using 150 GeV pions MC data. Only showers starting in the second layer are included.

In figure 5.10 longitudinal transition curves are shown for all pads. The numbering scheme of the pad is given in appendix C. The first layer is excluded since only showers starting in the second layer are included in the analysis. MC simulations for 150 GeV pions show (see figure 5.10) that more than 60% of the energy, which pions lose in the calorimeter, is deposited in the hit pad, and up to more than 90% in the central pads. The same amount of energy is deposited in pads 4 and 12. This is explained by the position of the beam spot, on the diagonal of the hit pad. Hence pads 4 and 12 are at equal distance from the the beam spot and on average, over many events, the same amount of energy is deposited. By excluding the outer pads only less than 10% of the energy reconstructed is lost. Therefore, only the four central pads are included in the analysis.

For pion data different procedures are used for the energy calibration of the hit pad and of the other central pads.

Hit pad

Using the measured data the pedestal and signal distributions are plotted for each layer. Like for the muon data the events with zero ADC counts are excluded. In order to choose the events starting in the second layer, cuts on the ADC counts (cut_{ADC}) are applied. They are determined by dividing the 0.35 GeV cut in energy by the corresponding muon calibration constant:

$$cut_{ADC,layer} = 0.35\,\mathrm{GeV}/C_{\mu,layer}. \tag{5.12}$$

The noise contribution is statistically subtracted and the mean value of the real signal is obtained (ADC_{hitpad}). The energy reconstructed for each layer is determined using the muon calibration constants according to:

$$E_{hit\,pad,layer} = C_{\mu,layer} \cdot ADC_{hit\,pad,layer}. \tag{5.13}$$

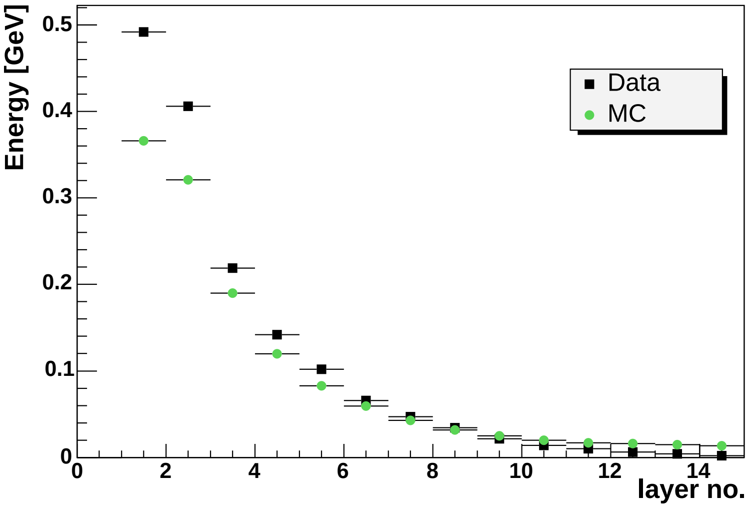

Figure 5.11: Comparison between the longitudinal energy distribution obtained from the MC simulation and from the measured data, for the hit pad. 150 GeV pion data have been used.

Figure 5.11 shows a comparison between the longitudinal energy distributions obtained from the MC simulation and from the measured data for all layers, except for the first layer since all showers included in the analysis start in the second layer. For layer two to layer nine the MC data underestimates the measured data. A possible explanation is a different position of the beam spot between data and MC. If the position of the beam spot in the experiment is further away from the center of the layer, hence from the other pads, more energy is deposited in the hit pad. The amount of energy deposited decreases with the depth of the shower. Therefore, the effect is more pronounced in the first layers. The percentage difference between the energy obtained from MC and from the measured data decreases from ~ 35% in layer two, to ~ 7% in layer nine. The error on the position of the beam spot is a source of a systematic error. Its effect on the longitudinal energy distribution curve and on the energy resolution will be discussed later in this chapter.

For layers 10 to 15 the MC data overestimates the measured data. The cut on the zero energy events introduces a bias. In MC this cut leads to an increase in the mean energy deposited. For the measured data the statistical subtraction of the noise corresponds to this cut. However, the increase in the mean energy is reduced by the muon contamination, which is not present in the MC.

Extension of the energy calibration to the other central pads

For the other central pads, a muon calibration could not be performed. Therefore, in order to obtain the energy calibration of these pads, the energy sharing between the hit pad and the other central pads is used.

Using the MC data 14 histograms are filled, for each of the central pads, starting with layer two. Two cuts are applied:

- one for choosing the starting layer as explained earlier,
- one against events with zero energy deposited.

In the case of the pion data there are events, in which the shower stops early, therefore no energy is deposited. This cut corresponds to the statistical subtraction of the noise for the measured data. The mean energy deposited is obtained ($E_{central\,pad}$). The following ratios are calculated:

$$R_{MC,central\,pad,\,layer} = \frac{E_{central\,pad,\,layer}}{E_{hit\,pad,\,layer}}, \tag{5.14}$$

which give the energy sharing between the hit and central pads in the MC.

For the measured data, the pedestal and signal distributions are plotted for each layer. Two cuts are applied:

- one against the events with zero ADC counts before pedestal subtraction, since at least an ADC value equal to the pedestal value should be recorded,
- one for choosing the starting layer.

With the first cut $\sim 43\%$ of the events are excluded and with both cuts $\sim 90\%$. In order to exclude the noise contribution to the signal, the statistical subtraction of the noise events is performed. The ADC count ratios are calculated:

$$R_{ADC,central\,pad,\,layer} = \frac{ADC_{central\,pad,\,layer}}{ADC_{hit\,pad,\,layer}}. \tag{5.15}$$

Having extracted the energy ratio from the MC and the ADC ratio from the data, the calibration constants are obtained according to:

$$C_{central\,pad,\,layer} = C_{\mu,\,layer}\frac{R_{MC,central\,pad,\,layer}}{R_{ADC,central\,pad,\,layer}}. \tag{5.16}$$

The energy reconstructed per layer is given by:

$$E^{rec}_{central\,pad,\,layer} = C_{central\,pad,\,layer} \cdot ADC_{central\,pad,\,layer}. \tag{5.17}$$

The errors on the $ADC_{central\,pad,\,layer}$ value are computed according to formula 5.8. For the errors of $R_{MC,central\,pad,\,layer}$, $R_{ADC,central\,pad,\,layer}$, $C_{central\,pad,\,layer}$ and

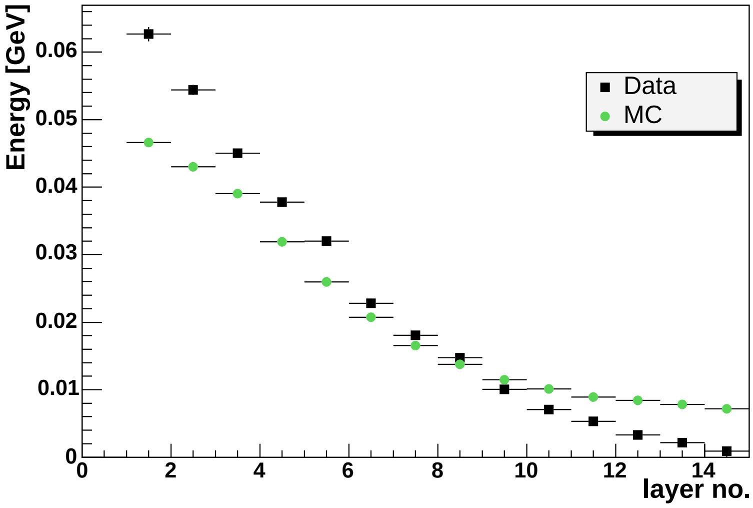

Figure 5.12: Comparison between the longitudinal energy distribution obtained from the MC simulation and from the measured data, for pad four. 150 GeV pion data have been used.

$E^{rec}_{central\,pad,\,layer}$ error propagation is applied. Table **??** gives the values and the errors for $E^{rec}_{central\,pad,\,layer}$ and $E_{central\,pad,\,layer}$.

Figure 5.12 shows a comparison between the longitudinal energy distribution obtained from the MC simulation and from the measured data, for pad four. The same behavior as for the hit pad is noticed. Up to layer nine the MC underestimates the data. The percentage difference decreases from $\sim$ 34.3% in the second layer to $\sim$ 7% in layer nine. For layers 10 to 15 the MC overestimates the data and the percentage difference increases from 12.7% in layer 10 to $\sim$ 87% in layer 15. The size of the errors is smaller than the marker size. They vary from $\sim$ 1% of the energy reconstructed in the first layers to $\sim$ 7% in the last layers. The absolute value decreases (see appendix G).

The position of the beam spot is a possible explanation for this difference. A systematic study is performed to determine the error it introduces on the energy resolution.

5.4 Energy resolution

All four central pads for all 14 layers have been calibrated. The next step is to obtain the energy resolution of the calorimeter.

Using formula 5.17 the energy reconstructed for each central pad is obtained. Then the energy in each layer is obtained by summing up the energies in the four central pads, according to:

$$E_{ij} = \sum_{c=1}^{4} E_{c,ij}, \tag{5.18}$$

where	i	is the event number,
	j	is the layer number and
	c	is the central pad number.

In order to determine the total energy deposited in the calorimeter (in the four central pads), the energy deposited in each layer is summed up:

$$E_{rec,i} = \alpha \sum_{j=1}^{15} C_j E_{ij}, \tag{5.19}$$

where i is the event number,
j is the layer number,
α is a global parameter, which accounts for the difference between the energy of the incoming particle and the energy deposited in the calorimeter and
C_j are individual parameters, different for each of the 15 layers.

The differences between the C_j parameters are due to the layer-to-layer effects like: different life time of the electron in TMP and different efficiencies of the chambers. The previous energy calibration accounts for most of the differences. However, residual effects are reflected in the C_j parameters. This procedure is applied for each event, i.e. the energy is reconstructed event by event. A Minuit [MIN98] fit program is used to minimize the χ^2 function:

$$\chi^2 = \sum_{i=1}^{N_{evt}} \frac{(E_{rec,i} - E_{beam})^2}{\sigma^2}, \tag{5.20}$$

where $E_{rec,i}$ is the energy reconstructed for event i,
E_{beam} is the energy of the beam and
σ is the error on the energy of the beam.

The error on the beam energy is less than 1%. For the fit σ was approximated to 1% .

The fit is performed in two steps.

- In the first step the values of the individual C_j parameters are fixed. The C_1 parameter is fixed to zero, since only events with showers starting in the second layer are considered. The other C_j (with j from 2 to 15) are fixed to 1. Thus, the global parameter α is fitted.
- In the second step the α parameter is fixed to the value obtained in the first step, C_1 is kept fixed as zero and the C_j $(2 \leq j \leq 15)$ parameters are fitted.

In order to verify that the fitting program works, the 150 GeV pion MC data are used. The results of the two steps are shown in figure 5.13. A Gaussian function is used to fit the distributions obtained. The parameters obtained from the fit are used to determine the energy resolution according to σ_E/E_{rec}, where E_{rec} and σ_E are the mean and sigma parameters of the Gaussian function.

An energy resolution of $9.76 \pm 0.10\%$ is obtained. The plots show an improvement after the second step. The value of the mean parameter increases by $\sim 1\%$ in the second step while the value of the sigma parameter decreases by $\sim 6.7\%$. This leads to an

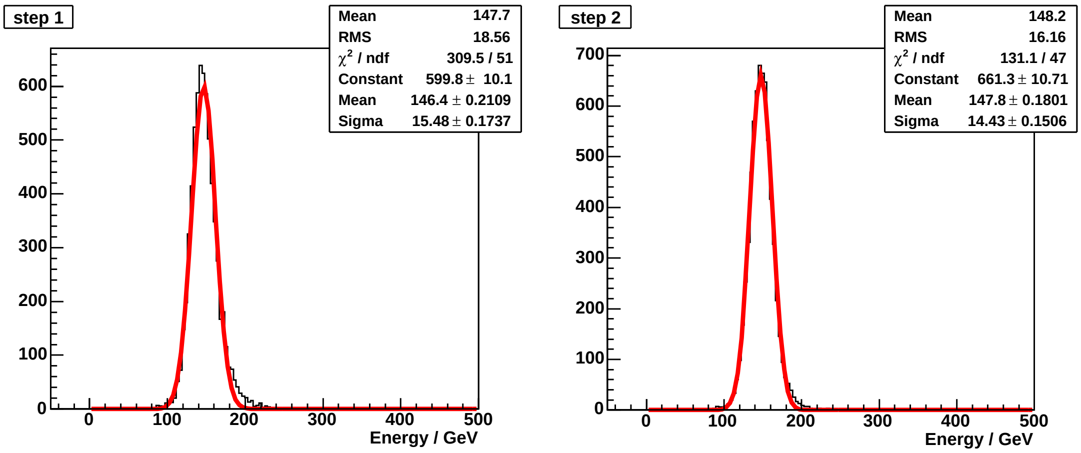

Figure 5.13: Energy resolution for 150 GeV pion MC data.

improvement of the energy resolution (σ_E/E_{rec}) in the second step of 7.4%. Still the value of the mean is less than 150 GeV, the energy of the particle. A possible source of this deviation is the lateral leakage. However, a study would be necessary to confirm it. Another reason is the asymmetry of the distributions. They show a small Landau like tail.

The MC data fit shows that the fitting program works. The next step is to apply it to the measured data. First the energy resolution of 150 GeV pion data is fitted. A negative $ADC_{central\,pad}$ is obtained for the last layer, pads 0 and 12. This leads to a negative $R_{ADC,\,layer}$ ratio and further to a negative energy reconstructed. Adding a negative energy makes no sense. A possible reason for this negative value of the data distribution after the pedestal subtraction is, that the p_0 overestimates the real value of the pedestal. The length of a hadronic shower increases logarithmically with the energy of the particle (see section 3.2). Hence, showers initiated by hadrons with an energy of 150 GeV or less will penetrate less deeply into the calorimeter. Therefore, little or no energy is deposited in the last layers of the calorimeter and the signal is dominated by noise. Subtracting a value for the pedestal higher than the real value can lead to a negative mean of the distribution. However, this behavior is not well understood and the decision to remove the entire last layer has been taken.

Therefore, in the fitting program the C_{15} parameter is fixed to zero, which is equivalent to zero energy deposited in this layer. The result of the fit for 150 GeV pion data, for both steps, is shown in figure 5.14. An energy resolution of $(24.40 \pm 0.74)\%$ is obtained. The behavior is similar to the one observed in the MC data. In the second step the mean parameter increases by $\sim 3.3\%$, the sigma parameter decreases by $\sim 6.3\%$ and the energy resolution improves by $\sim 9.4\%$. The mean parameter has a value (137.5 ± 1.12) GeV, 8.3% less than the target 150 GeV. Like in the case of MC data the asymmetry of the distribution is one of the reasons. Due to the noise, which is not present in MC data, the sigma of the distribution increases by $\sim 130\%$. Hence the energy resolution is worse than in the case of the MC data.

The same procedure is applied for all data energies. Three other examples are presented in appendix D for pion data taken at energies of 30 GeV, 100 GeV and 200 GeV.

For energies greater than 150 GeV all layers are included in the analysis. At these

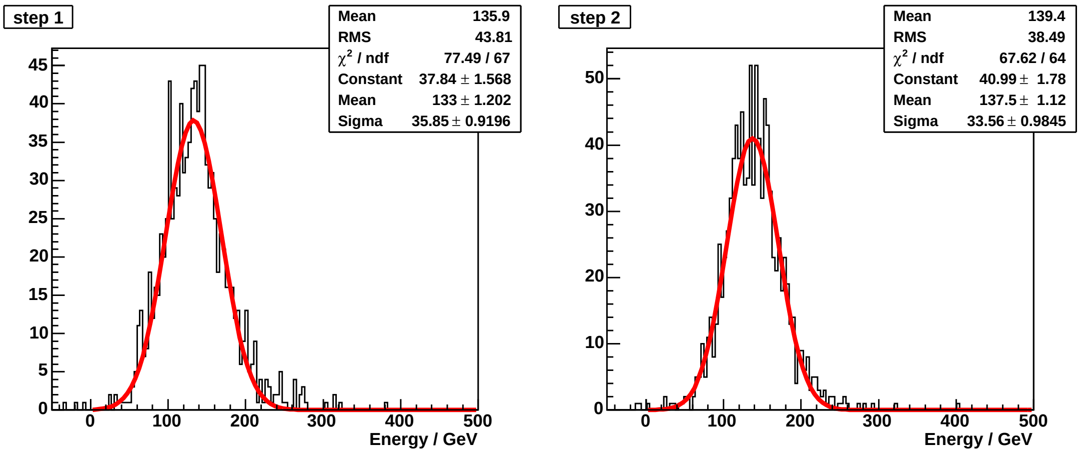

Figure 5.14: Energy resolution for 150 GeV pion data.

energies the particle shower reaches the last layer. The amount of energy deposited increases with the energy. For energies smaller than 150 GeV negative $R_{ADC,layer}$ ratios are obtained for the last layers. A layer is excluded from the analysis if for at least one central pad the mean of the data distribution (pedestal subtracted) is negative. The number of layers included N_{in} decreases with energy from 13 layers at 150 GeV to 5 layers at 15 GeV. For energies greater than 150 GeV all 14 layers are included. The first layer is excluded since only events with showers starting in the second layer are included. In the fitting program all C_j parameters corresponding to the excluded layers are fixed to zero.

Energy [GeV]	N_{in}	E_{rec}[GeV]	σ_E[GeV]	σ_E/E_{rec}
15	5	10.25 ± 0.43	5.55 ± 0.40	(54.21 ± 4.56) %
30	7	23.93 ± 0.36	9.71 ± 0.29	(40.60 ± 1.37) %
50	11	44.18 ± 0.46	14.24 ± 0.40	(32.23 ± 0.97) %
100	12	91.55 ± 0.87	24.67 ± 0.71	(26.94 ± 0.81) %
150	13	137.50 ± 1.12	33.56 ± 0.98	(24.40 ± 0.74) %
200	14	189.0 ± 1.10	37.30 ± 0.88	(19.73 ± 0.48) %
250	14	240.70 ± 1.86	39.10 ± 0.89	(16.24 ± 0.39) %
300	14	285.10 ± 1.33	44.65 ± 1.12	(15.66 ± 0.40) %
350	14	335.10 ± 1.37	46.29 ± 1.02	(13.81 ± 0.30) %

Table 5.1: Values of the reconstructed energy mean, the sigma of the distribution and the energy resolution. The number of layers included in the analysis, starting with layer two, are also given. The values are obtained using the Minuit based program for pion data with energies from 15 GeV to 350 GeV.

Table 5.1 gives the values for σ_E, E_{rec}, σ_E/E_{rec} and the numbers of layers included in the analysis, starting with layer two, for all data energies. The errors on σ_E and E_{rec} are the errors obtained by fitting the distributions with a Gaussian function. The errors on σ_E are computed according to the error propagation formula. As expected, the energy resolution improves with energy, from 54.21% at an energy of 15 GeV to 13.81% at an energy of 350 GeV.

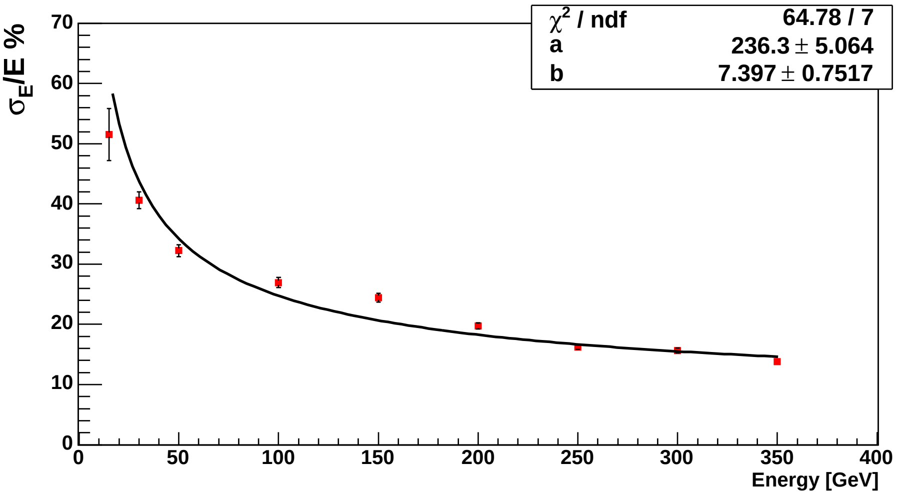

Figure 5.15: Energy resolutions for energies from 15 GeV to 350 GeV. Formula 5.21 is used to fit the points.

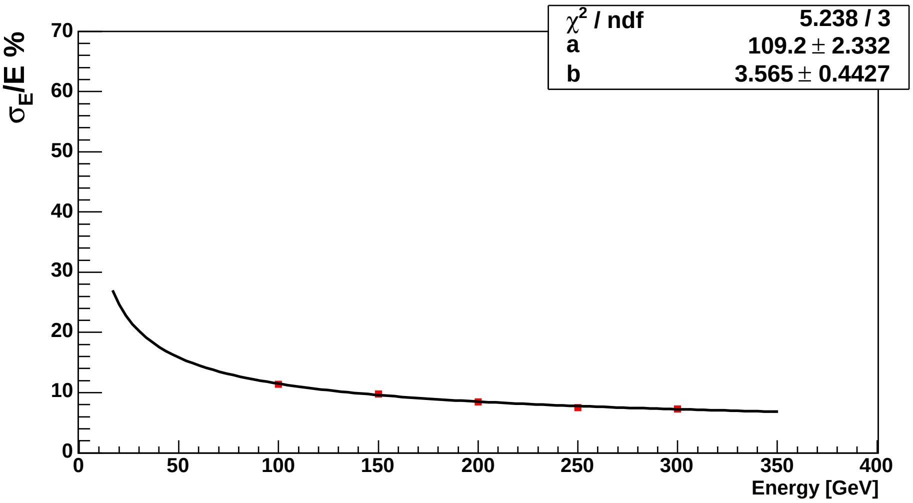

Figure 5.16: Energy resolutions for energies from 100 GeV to 300 GeV, using MC data.

The energy resolutions are plotted in figure 5.15. The following formula:

$$\frac{\sigma(E)}{E} = \frac{a}{\sqrt{E\,[\mathrm{GeV}]}} \oplus b, \tag{5.21}$$

is used to fit the points.

The following results are obtained for the parameters.

- The sampling term $a = (236.3 \pm 5.06)\,\%$. It includes the sampling and the statistical fluctuation in the shower development. It has a $1/\sqrt{E}$ dependence. Therefore, at high energies it has a small contribution to the energy resolution.

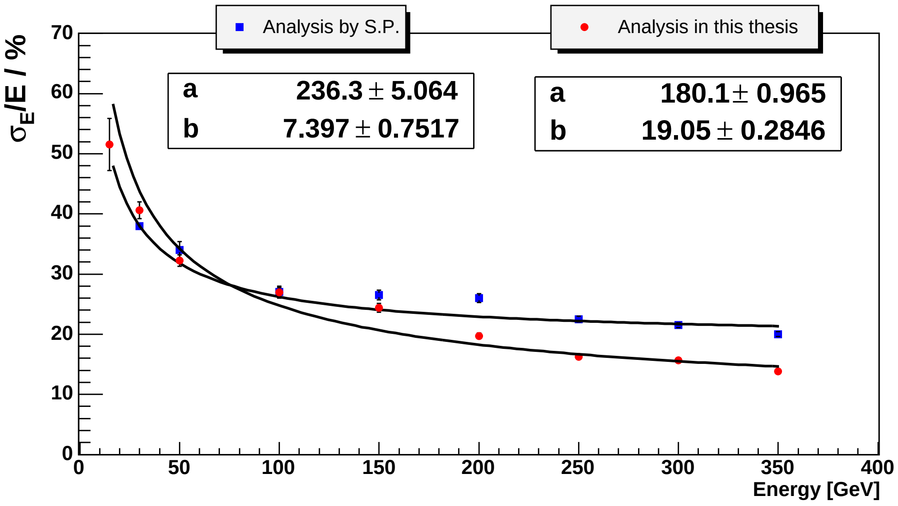

Figure 5.17: Comparison of energy resolution results of parallel analysis [Ple04] on the test-beam data.

- The constant term $b = (7.40 \pm 0.75)\,\%$. It is energy independent. Thus it dominates the energy resolution at high energies.

In figure 5.16 the energy resolutions at energies from 100 GeV to 300 GeV, obtained by using MC simulations, are shown. As expected both the sampling and constant terms are better than for the measured data.

The data have been analyzed in parallel by another group [Ple04]. A comparison of the energy resolution obtained in this analysis and the preliminary result of the parallel analysis is shown in figure 5.17. The results of this analysis show a lower energy resolution at energies below 100 GeV. This is reflected in the sampling term, which is 30% larger compared to the sampling term in the parallel analysis. At energies higher than 100 GeV the energy resolution is better, reflected in the constant term, which is 60% lower compared to the results of the parallel analysis.

In conclusion, the energy resolution has been obtained for all data points up to energies of 350 GeV. At low energies the result is dominated by the sampling fluctuations. The higher the energy of the incident particle, the smaller the contribution of the sampling fluctuations, and the energy resolution increases. At high energies the constant term dominates.

The KASCADE-Grande hadron calorimeter is intended to measure hadrons with higher energies (in the TeV range). Therefore, it is important to obtain a constant term as small as possible.

5.5 Systematic studies

5.5.1 Statistical subtraction of the noise contribution

In order to exclude the noise contribution from the signal, a statistical subtraction has been used. The procedure is described in detail in section 5.2.1 and is a source of systematic errors. This method is used for both the calibration of the hit pad with muon data and the calibration of the other central pads using pion data. Thus two systematic studies have to be done. 100 GeV muon and 150 GeV pion data are used.

Muon calibration of the hit pad

In order to determine the number of noise events in the signal a Gaussian function is used to fit the noise distribution. The amplitude parameter of this fit gives the number of noise events. The range, in which the distribution is fitted, is fixed. The choice of the range effects the amplitude and thus the number of noise events. Therefore, the choice of the range is a source of systematic errors.

The possible systematic error on the final result has to be determined. First the range is varied with $\pm 1\sigma$ of the width of the pedestal distribution. This procedure is done for each layer separately, i.e. the value of the sigma is given by the pedestal distribution in the corresponding layer. The changes obtained are shown in table E.1. The percentage values of the changes vary from layer to layer in a range from $\sim 0.2\%$ to $\sim 15.8\%$. To be conservative, a global change of ±15% in the number of noise events has been chosen for all layers. This results in a variation of the muon calibration constants of less than 1.5% for all layers. Table 5.2 gives the values obtained for the calibration constants and differences in percentage.

Lay. no.	$C_{\mu,layer}/10^{-4}$	$C^{-15\%}_{\mu,layer}/10^{-4}$	diff	$C^{+15\%}_{\mu,layer}/10^{-4}$	diff
1	6.35 ± 0.05	6.40 ± 0.05	-0.84%	6.30 ± 0.05	0.84%
2	3.78 ± 0.03	3.80 ± 0.03	-0.58%	3.76 ± 0.03	0.58%
3	2.58 ± 0.02	2.60 ± 0.02	-0.53%	2.57 ± 0.02	0.53%
4	2.81 ± 0.02	2.83 ± 0.02	-0.55%	2.79 ± 0.02	0.55%
5	6.80 ± 0.07	6.86 ± 0.07	-0.89%	6.73 ± 0.07	0.89%
6	4.92 ± 0.05	4.96 ± 0.05	-0.86%	4.88 ± 0.05	0.74%
7	2.71 ± 0.02	2.73 ± 0.02	-0.64%	2.69 ± 0.02	0.64%
8	4.14 ± 0.04	4.18 ± 0.04	-0.84%	4.11 ± 0.04	0.84%
9	8.63 ± 0.09	8.75 ± 0.09	-1.33%	8.52 ± 0.09	1.33%
10	4.74 ± 0.04	4.78 ± 0.04	-0.86%	4.70 ± 0.04	0.86%
11	2.92 ± 0.02	2.93 ± 0.02	-0.64%	2.90 ± 0.02	0.64%
12	3.63 ± 0.03	3.66 ± 0.03	-0.81%	3.60 ± 0.03	0.81%
13	5.25 ± 0.05	5.30 ± 0.05	-0.85%	5.21 ± 0.05	0.85%
14	3.77 ± 0.03	3.79 ± 0.03	-0.67%	3.74 ± 0.03	0.67%
15	4.67 ± 0.04	4.70 ± 0.04	-0.72%	4.63 ± 0.04	0.72%

Table 5.2: Changes in the value of the muon calibration constants due to changes in the number of noise events of ±15%.

Using the new muon calibration constants $C^{-15\%}_{\mu,layer}$ and $C^{+15\%}_{\mu,layer}$, for the rest of the analysis, gives no change in the final result, i.e. on the energy resolution. There is a small change of $\sim 0.2\%$ in the energy resolution after the first step of the fitting program. In this step only the α parameter is free. In the second step the C_j parameters are left free and the changes in the values of the muon calibration constants are compensated by changes in the values of the C_j fit parameters (see table E.2) .

Conclusion: a change of ±15% in the number of noise events does not introduce an error on the energy resolution. Thus, using the method of statistical subtraction of the noise for the muon calibration of the hit pad is not a source of systematic errors.

Pion calibration of the other central pads

The statistical subtraction of the noise events in the signal is used in the case of pion data as well. Thus, a similar study of systematic errors is performed.

First, the range is varied with $\pm 1\sigma$ of the width of the pedestal distribution. This is done for all central pads. The values obtained for the number of noise events in the signal, for the hit pad and for pad four, are given in appendix F.

For a change of -1σ the percentage differences vary from $\sim 24\%$ to less than 1% of the number of noise events. The large percentage differences are found in the first layers, where there is a large amount of energy deposited and the number of noise events is less than 20. Thus a high percentage difference is produced by a change of only a few events. The average differences for all layers are $\sim 8\%$ for the hit pad and $\sim 5\%$ for pad four. For the rest of the study a change of +10% in the number of noise events is chosen.

When a change of $+1\sigma$ is applied, the percentage differences for 6 of the layers are less than −1% and for all layers an average of $\sim -3\%$ is obtained for the hit pad and of $\sim -1.5\%$ for the other central pad. To be conservative a change of −5% in the number of noise events is chosen.

	E_{rec} [GeV]	σ_E [GeV]	σ_E/E_{rec}
+10%	137.5 ± 1.12	33.58 ± 0.98	$(24.42 \pm 0.74)\,\%$
	137.5 ± 1.12	33.56 ± 0.98	$(24.40 \pm 0.74)\,\%$
−5%	137.5 ± 1.21	33.55 ± 0.98	$(24.4 \pm 0.74)\,\%$

Table 5.3: Values of the energy mean, the sigma of the energy distribution and the energy resolution for a change in the number of noise events by +10% and −5%.

The results obtained by changing the number of noise events by +10% and −5% are given in table 5.3. There is no change in E_{rec} and the changes on σ_E are less than the statistical errors. The systematic errors introduced on the energy resolution are within the statistical errors.

5.5.2 Position of the beam spot

In the MC simulation the position of the beam spot is fixed 4 cm to the left and 4 cm below the center of the calorimeter. For the measured data there is an error on the beam spot. Two plastic scintillators are used in coincidence to provide a trigger. The sensitive area is $10 \times 10\,\mathrm{cm}^2$. As a consequence the position of the beam is known within this area. The trigger panel was centered 4 cm to the left and 4 cm below the center of the first layer. Thus, there is an error of ±5 cm on the beam spot. The error on the accuracy of the alignment of the panels also adds up. In order to study the effect on the energy resolution, MC simulations are used. The entrance point of the primary particle is changed to several positions on the diagonal of the hit pad. For a more thorough study positions outside the diagonal may also be considered.

The values obtained for the energy resolution are presented in table 5.4. Changing the entrance point of the particle on the diagonal by +4 or −2 cm gives a maximum improvement in the energy resolution of less than 1%.

Position [cm]	E_{rec} [GeV]	σ_E [GeV]	σ_E/E_{rec}
2, -2	137.8 ± 1.13	34.23 ± 0.97	$(24.84 \pm 0.73)\,\%$
3, -3	137.7 ± 1.12	33.52 ± 1.02	$(24.34 \pm 0.76)\%$
4, -4	137.5 ± 1.12	33.56 ± 0.98	$(24.40 \pm 0.74)\,\%$
5, -5	137.7 ± 1.11	33.68 ± 0.92	$(23.73 \pm 0.69)\,\%$
6, -6	137.8 ± 1.09	32.91 ± 0.86	$(23.88 \pm 0.65)\,\%$
8, -8	137.2 ± 1.12	33.08 ± 0.89	$(24.11 \pm 0.68)\,\%$

Table 5.4: Values of the reconstructed energy, the sigma of the energy distribution and the energy resolution for different positions of the beam spot in the MC. All values are obtained for 150 GeV pion data.

Changes in the energy longitudinal distribution due to a change in the beam position 5 cm to the left and 5 cm below the center of the layer, are shown in figure G.2. In addition values of the normalized ratio $(E_{Data} - E_{MC})/E_{MC}$ are shown for positions 4 and 5 cm below and at the left of the center of the layer. An improvement is noticed for the later. The errors on the points are in the order of 10^{-3} – 10^{4}.

5.5.3 Stability with time

The time stability within one run has been checked by checking the pedestal stability. In order to check the stability of the energy resolution with time over several runs, two runs, which have been recorded four hours apart, are used. The values obtained for the energy resolutions are given in table 5.5. The differences between the two runs are within the statistical errors.

Run number	E_{rec} [GeV]	σ_E [GeV]	σ_E/E_{rec}
Run 123	91.55 ± 0.87	24.67 ± 0.71	$(26.94 \pm 0.81)\,\%$
Run 120	90.66 ± 0.86	23.6 ± 0.68	$(26.03 \pm 0.79)\,\%$

Table 5.5: Values of the reconstructed energy, the sigma of the energy distribution and the energy resolution for two different runs, recorded four hours apart (100 GeV pions).

5.5.4 Estimate of the pedestal value

As an estimate of the pedestal value the p_0 parameter has been chosen. The distribution of the differences between the p_0 parameter and the mean of the pedestal distribution m_{ped} for all 240 channels is shown in figure 5.2. The sigma parameter obtained by fitting this distribution with a Gaussian function gives the error introduced by using p_0 instead of m_{ped}.

For this study a variation of the value of the p_0 parameter of $\pm 3\sigma$ of the above distribution is chosen. The values obtained for the energy mean, the sigma of the distribution and the energy resolution are given in table 5.6.

	E_{rec} [GeV]	σ_E [GeV]	σ_E/E_{rec}
-3σ	137.6 ± 1.11	33.48 ± 0.97	(24.33 ± 0.73) %
	137.5 ± 1.12	33.56 ± 0.98	(24.40 ± 0.74) %
$+3\sigma$	137.3 ± 1.08	33.36 ± 0.90	(23.56 ± 0.68) %

Table 5.6: Values of the reconstructed energy, the sigma of the distribution and the energy resolution obtained by changing the pedestal value by $\pm 3\sigma$ (150 GeV pions).

For a variation of -3σ in the value of p_0, both the mean and the sigma increase, however the change in the energy resolution is less than the statistical errors. For a variation of $+3\sigma$ both the mean and the sigma decrease. There is a tendency of the energy resolution to increase, but more statistic is needed to clarify this.

5.5.5 Events outside the linear part of the calibration curve of the electronic chain

The electronic chain has a nonlinear characteristic curve (see figure 4.5) with a linear part in the low ADC count range. Typically this extends to ~ 4000 ADC counts. For most of the events the ADC counts recorded are in this low ADC counts range. However, at energies above 100 GeV events outside the linear part have also been recorded. In the analysis no special correction has been applied for these events. This is a source of systematic errors and the effect on the energy resolution is studied.

The u_1 parameter in formula 4.8 gives the limit between the linear and nonlinear part of the characteristic curve. Using the value of this parameter as a cut on the value of ADC counts recorded, the number of events outside the linear part is obtained ($N_{ev,NL}$).

Energy[GeV]	$N_{ev,total}$	$N_{ev,NL}$	$N_{ev,NL}$ [%]
350	113 340	12 498	11
300	110 135	8 901	8
250	115 553	5 219	4.5
200	110 616	2 349	2.1
150	111 998	1 088	1
100	110 657	122	0.1

Table 5.7: Values of the total number of events recorded ($N_{ev,total}$) and the number of events outside the linear part ($N_{ev,NL}$), the absolute value and the percentage.

Table 5.7 gives the absolute numbers and the percentages of these events, for primary energies higher than 100 GeV. The numbers presented here are obtained for the hit pad in layer three. For the other pads the percentages are lower, since most of the energy is deposited in the hit pad. The highest percentage is recorded at 350 GeV, since the amount of energy deposited, hence the ADC count value read, increases with the energy of the primary particle. The largest error introduced by not correcting for these events will be found at this energy. Thus, 350 GeV pion data are used for this study.

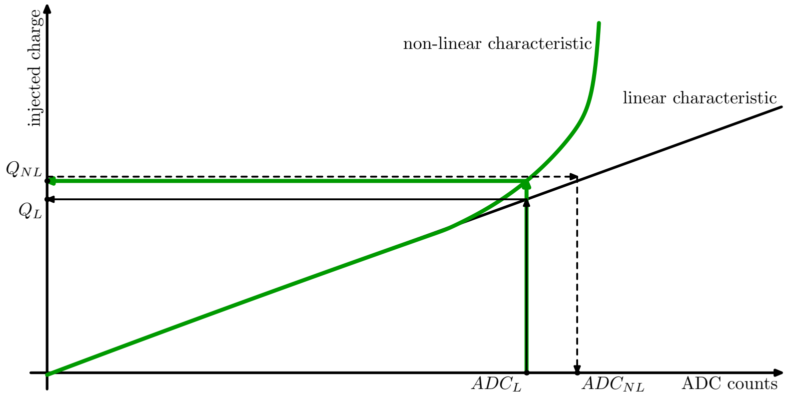

Figure 5.18: Correction of the ADC count value from the recorded ADC_L, corresponding to a linear characteristic, to ADC_{NL} corresponding to the nonlinear characteristic. For a more detail discussion see the text.

As shown in figure 5.18, an ADC value (ADC_L) corresponds to a charge Q_L given by:

$$Q_L = Q_1(ADC_L), \tag{5.22}$$

where $Q_1 = p_1(x - p_0) + p_2(x - p_0)$ (see formula 4.8).

If a nonlinear characteristic is assumed, then the same ADC_L value corresponds to a charge:

$$Q_{NL} = Q(ADC_L), \tag{5.23}$$

where $Q(x)$ is the function, which parameterizes the nonlinear characteristic curve of the electronic chain (formula 4.8). Hence, the corrected ADC count value (ADC_{NL}) is given by:

$$ADC_{NL} = Q_1^{-1}(Q_{NL}). \tag{5.24}$$

The p_2 parameter has values $\sim 10^{-6}$. The p_1 parameter has a value $\sim 10^{-1}$. Therefore, the second term in the Q_1 function can be neglected. This leads to:

$$ADC_{NL} = p_0 + \frac{Q(ADC_L)}{p_1}. \tag{5.25}$$

The values of the 12 parameters of the function $Q(x)$ are taken from the electronic calibration data. The Minuit based fit is used to fit the energy reconstructed using the corrected ADC values.

The values obtained for the energy resolution are presented in table 5.8.

There is a slight increase of $\sim 0.1\%$ in the energy mean, but the increase of the sigma is larger $\sim 0.5\%$. Hence, the energy resolution decreases by $\sim 0.4\%$, but this change is not really significant.

	E_{rec} [GeV]	σ_E [GeV]	σ_E/E_{rec}
Without correction	335.1 ± 1.37	46.29 ± 1.02	$(13.81 \pm 0.30)\,\%$
With correction	335.5 ± 1.38	46.54 ± 1.04	$(13.87 \pm 0.31)\,\%$

Table 5.8: Values of the reconstructed energy, the sigma of the distribution and the energy resolution obtained with and without applying a correction for the events outside the linear part of the characteristic curve of the electronic chain. The 350 GeV pions data from Run 119 have been used.

5.5.6 Total systematic error

An overview of the systematic errors on σ_E/E_{rec} 150 GeV for pion data are presented in table 5.9. The systematic error due to event outside the linear characteristic of the electronic chain is overestimated, since it was obtained for 350 GeV pion data.

Systematic study	Error [%]
Statistical subtraction	
of noise events for muon data	0.00
of noise events for pion data	0.02
Position of the beam spot	0.67
Stability with time	0.91
Estimate of the pedestal value	0.84
Events outside the linear part of the characteristic curve of the electronic chain	0.06
Total systematic error (added in quadrature)	1.4

Table 5.9: Summary of the systematic studies performed and values of the systematic error obtained.

Hence the energy resolution for 150 GeV pion data is:

$$\frac{\sigma_E}{E}(150\,\mathrm{GeV}) = (24.40 \pm 0.74 \pm 1.4)\,\%. \tag{5.26}$$

5.6 Discussion of the results and possible improvements

The steps of the analysis can be summarized as follows.

- The pedestal value and its stability with time have been determined. As an estimate for the pedestal value the p_0 parameter has been chosen. Studies have shown that the systematic error on the energy resolution introduced by using this value is less than the statistical error.

- The calibration of the central pads has been obtained using 100 GeV muon data for the hit pad and 150 GeV pion data for the other central pads. In order to exclude the noise contribution to the signal a statistical subtraction method has been used. The systematic uncertainties of this method are again within the statistical errors.

- The energy resolution of the calorimeter has been obtained:

  $$\frac{\sigma_E}{E} = \frac{(236.30 \pm 5.06)\%}{\sqrt{E}} \oplus (7.40 \pm 0.75)\%. \tag{5.27}$$

  Taking into account that the KASCADE-Grande calorimeter is intended to measure hadrons with energies up to the TeV range, the calorimeter provides adequate, good energy resolution. At these high energies the constant term dominates the energy resolution.

During this chapter several possible improvements have been indicated.

- A possible way to improve the method used to exclude the noise contribution is by fitting the shape of the distribution. Therefore, a function which describes both the muon and pion distributions has to be found.
- In order to exclude the muon contamination in the pion data additional studies have to be performed. MC simulations, in which a similar contamination is introduced, may be helpful to develop a procedure.
- Using the MC simulation, with different impact spots, the beam position has to be determined as well as possible for each data run. This may also improve the agreement of the longitudinal transition curves for the first layers.
- A possible way to improve the energy resolution, for high energies pion data, is by including some of the other pads in the analysis. This will increase the amount of energy reconstructed. However, at low energies this will only introduce noise, thus decrease the resolution.

Chapter 6

Summary

The iron sampling calorimeter of the KASCADE-Grande experiment is the largest installation, which uses a warm liquid as medium in ionisation chambers. It is used to measure single hadrons and to determine their energies and directions. In order to obtain a data-based energy calibration, a testbeam calorimeter has been built and tested at CERN in 2003. In this thesis the performance of the testbeam calorimeter has been studied.

The testbeam calorimeter consists of 15 layers of liquid ionization chambers filled with TMP. In between these layers 13 layers of iron absorber are placed. In addition one layer of lead absorber is installed behind the first layer of liquid ionization chambers.

The data acquired during the testbeam period have been analyzed. The goal was to determine the energy resolution of the calorimeter for hadrons at energies between 15 and 350 GeV. First, the stability of the pedestal has been established. In order to estimate the value of the pedestal, a value for the entire run per pad, obtained from the electronic calibration, has been used.

Using 100 GeV muon data, the energy calibration of the hit pad has been obtained. In order to exclude the noise contribution to the signal, a statistical subtraction of the noise events has been performed. A good agreement has been found between the muon energy reconstructed and the muon energy obtained using Monte Carlo simulations employing the GEANT/FLUKA code.

Using 150 GeV pion/proton data, the energy calibration of the other central pads has been performed. Like for the muon data a statistical subtraction method has been used to exclude the noise contribution to the signal. In order to determine the calibration constants, a method based on the energy sharing between the hit pad and the other central pads has been used. Longitudinal energy distribution curves have been obtained for all central pads and comparisons with results of Monte Carlo simulation have also been shown. The values of the energy reconstructed compared to the energy obtained from Monte Carlo simulation is larger in the calorimeter layers 2 to 9 and smaller in layers 10 to 15.

The energy resolution has been obtained for pions with energies from 15 to 350 GeV. The final result, the energy resolution of the testbeam calorimeter, is given by:

$$\frac{\sigma_E}{E} = \frac{236.30\%}{\sqrt{E}} \oplus 7.40\%.$$

The small constant term is important for the application in the KASCADE-Grande calorimeter, where particles with typical energies considerably high, up to the TeV range, are measured.

Systematic studies have been performed for the uncertainty introduced by statistically subtracting the noise events, in muon and pion data, and for the influence of the nonlinearity of the electronic calibration curve at high energies. The systematic errors obtained are considerably smaller than the statistical error. The systematic errors for the uncertainty in the knowledge about the correct beam position, for the deviation between the true and the estimated value of the pedestal and for the time stability of the energy resolution, have also been determined. Their values are comparable to the value of the statistical error. The total systematic error has been obtained for 150 GeV pion/proton data:

$$\frac{\sigma_E}{E}\,(150\,\mathrm{GeV}) = (24.40 \pm 0.74\,(stat) \pm 1.40\,(syst))\,\%\,.$$

A value of the systematic error two times larger than the value of the statistical error, has been found.

Appendix A

List of all runs

A.1 First period

Energy [GeV]	Run no. (no. of events)	Good(G)/ Bad(B)	Comments
5000V/π/p			
15	74 (38.073k)	B	fluctuating rate, transition curve shows e
	77 (22k)	B	SPS Booster problems
	84 (10.048k)	G	Combine 84 and 85
	85 (33.624k)	G	
30	75()	B	Trig1(10mm Pb absorber) missing
	76 (38.692k)	B	Broad beam, second. Particles
	69 (30.83k)	B	Unable to increase the rate
	70()	B	Unstable data(BEND 7 problems)
	81 (35.019k)	B	Rate increase from 300 to 800, B7 probl
	82()	B	Test run
	83 (85.909k)	G	
50	6 (4.595 k)	B	Crane activity
	7 (24.5 k)	B	Crane activity
	8 ()	B	5 part/spill
	16 (40 k)	B	Instable beam
	17(112.421 k)	G	
100	5 (64 k)	G	
	18 (131.6 k)	G	
150	2(51.56 k)	B	Electron contaminated
	9 ()	B	Beam tuned by operator
	10 (100.534k)	G	1180 recorded
	19 (116.7 k)	G	
5000V/π/p			
200	4 (50.805 k)	G	
	11 ()	B	- triger window changed, NIM crate problem
	12 ()	B	- didn't get any data, NIM crate problem
	13 ()	B	- electronic problems, NIM crate problem
	14 ()	B	- no particles any more (BEND 7 problems)
	15 (108 k)	G	
	20 (113.3k)	G	

Energy [GeV]	Run no. (no. of events)	Good(G)/ Bad(B)	Comments
	23 (4.175k)	B	3xcoincidence attempted,170part/spill unknown particles
250	3 (0.250k)	B	Low statistic
	21 (112.4 k)	G	
300	22 (112 k)	G	
5000V/e$^-$			
15	34 (111.105k)	B	Temporary no beam
	80 (23.518k)	B	rate decresed from 1200 to 80, second. Particl.
30	35 (120.485k)	B	Moving colimator, 3.5e+3/spill
	79 (148.548k)	G	
50	36 (111.124k)	B	Rate decresed from 3.5e+3 to 1.7e+3 secondary particles
	71 (36.711k)	B	1.6e+5 p/spill,withmed. cam. in front
	72 (), target Pb	B	2.1e+5 p/spill, 25 mm Pb with med. cam. in front
	78 (119.469k)	G	
100	31 (38.971k)	B	data taken while ops. Optimize rate, don't know what part. rate increased 130-¿450, target Pb
	32 (43k), target Pb	B	after tuning
100	33 (112.558), target Pb	B	after tuning, 800 events/spill, see31
	73()	B	1.1e+4 p/spill, 25mm Pb with med. cam. in front
150	27 (113.556k)	G	target air
200	28()	B	Wrong keyboard input cancelled
	29 (112.714k)	G	target air
250	30(110.462k)	G	target air
5000V / μ			
150	24 (11.207k)	G	190part/spill
	25(14.351)	G	SPS problems(no beam)
	26 (84.86k)	G	

A.2 Second period

Energy [GeV]	Run no. (no. of events)	Good(G)/ Bad(B)	Comments
5000V/π/p			
15	133 (59.172k)	G	210/spill
	134 (35.484k)	G	200/spill
30	111(1.368k)	G	1400/spill
	122 (1.206k/119.819k)	G	1500/spill
50	121 (1206k)	G	
	124 (114.519k)	G	π^+

Energy [GeV]	Run no. (no. of events)	Good(G)/ Bad(B)	Comments
100	120 (120.6k)	G	
	123 (110.657k)	G	π^+
150	115 (111.998k)	G	Test run ,5800/spill, π^+
200	116 (110.616k)	G	5000/spill, π^+
250	117 (115.553k)	G	3000/spill, π^+
300	118 (110.135k)	G	4700/spill, π^+
350	110()	B	π^+
	119 (113.34k)	G	3500/spill, π^+
		5000V/μ	
50	113 (25.31k)	B	Comp. Probl.(data lost),2600/spill
	114 (112.43k)	G	Crane activity
100	125 (148.840k)	G	3500/spill, π^+
150	126 (194.576k)	B	Low ped., 2300/spill, π^+
200	127 (132.287k)	G	3600/spill
250	128 (187.890k)	G	3500/spill
		5000V/e$^-$	
15	132 (126.534k)	B	Ped. Probl. In one ch., 3100/spill
30	129 (133.64k)	G	3300/spill
50	130 (115.068k)	G	3800/spill
100	131 (130.943k)	G	4500/spill
150			
200			
250			
		4000V/ π/p	
15	90 (4.853k), Pb	G	2 channels with low pedestal,150/spill
	91 (85.04k), Pb	G	150/spill
	100 (11.114k)	G	130/spill
	101 (14.155k)	G	
30	89 (121.905k), Pb	G	1500/spill
50	88 (118.56k), Pb	G	2300/spill
100	92 (110.167k), Pb	G	300/spill
150	93 (110.408k), Pb	G	3600/spill
200	99 (106.274k)	G	2500/spill, π^+
	94 (113.716k), Pb	G	2 ch. With low pedestal, 2400/spill
250	95 (110.807k), Pb	B	High ped., 2200/spill, π^+

Energy [GeV]	Run no. (no. of events)	Good(G)/ Bad(B)	Comments
300	96 (121.3832k), Pb	G	6000/spill, π^+
350	97 (123.072k), Pb	G	3700/spill, π^+
		4000V/μ	
50	98 (110.131k)	G	1500/spill, π^+
		4000V/e$^-$	
50	86(75.045k)	B	target Pb
	87(84.573k)	G	target Pb, 5500/spill
	102(148.221k)	B	With med. Cam.
		4300V/e$^-$	
50	103(89.418k)	B	With med. Cam.
	104(90.915k)	B	With med. Cam.
	105(92.447k)	B	With med. Cam.
		4400V/e$^-$	
50	106(490k/92.514k)	B	With med. Cam.
		4500V/ π/p	
30	111(136.849k)	G	Instable B9,1400/spill
150	1()		Test run
350	110(114.563k)	G	3800/spill, π^+
		4500V/ μ	
50	112(126.302k)	G	2500/spill, π^+

Appendix B

Shower examples

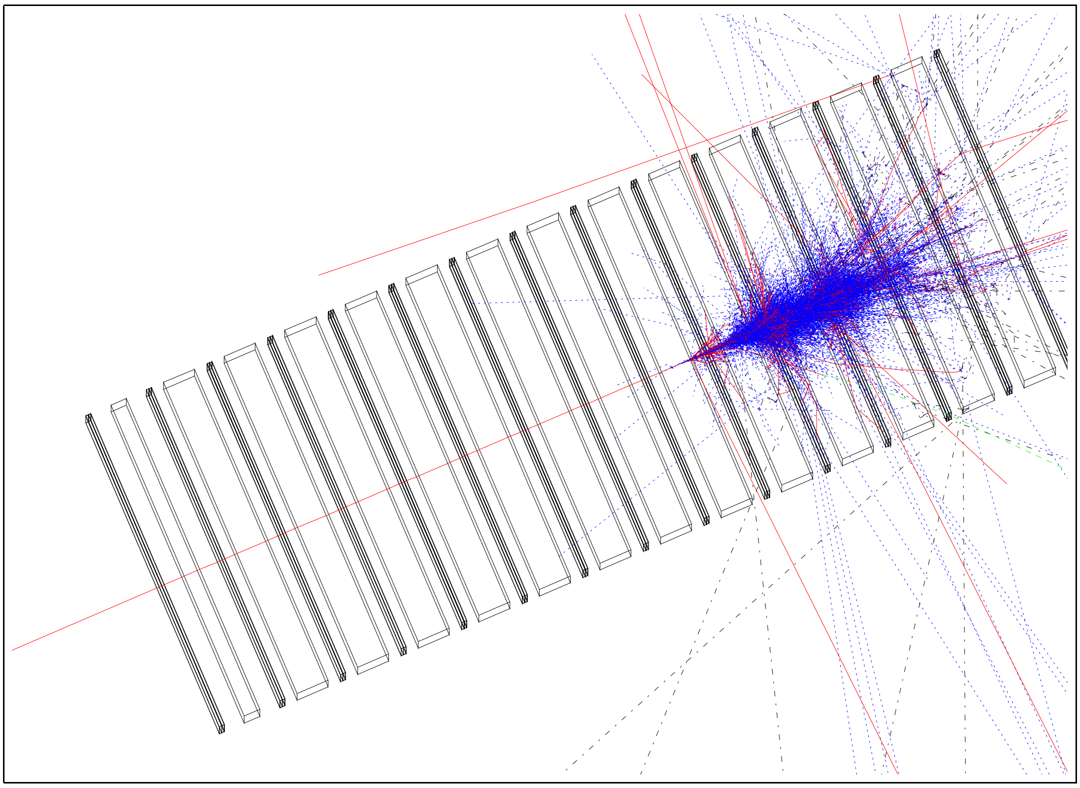

Figure B.1: Display of an event with shower starting after layer seven.

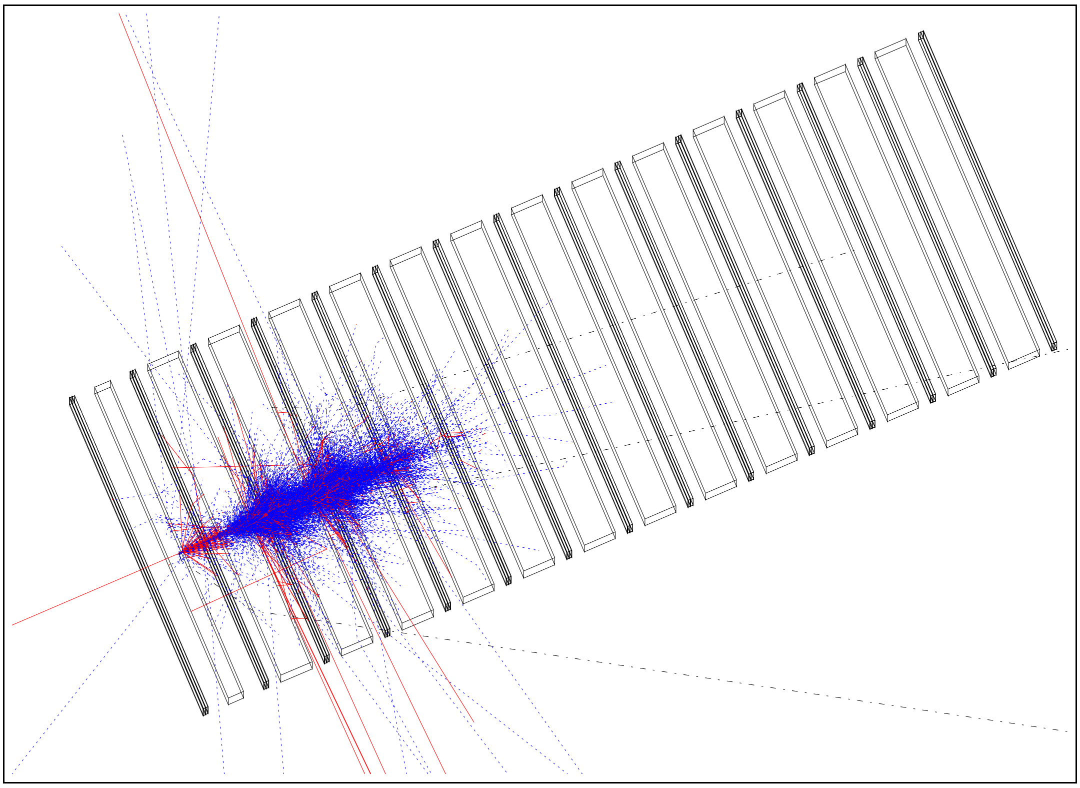

Figure B.2: Display of an event with shower ending before layer seven.

Appendix C

Numbering scheme of the pads

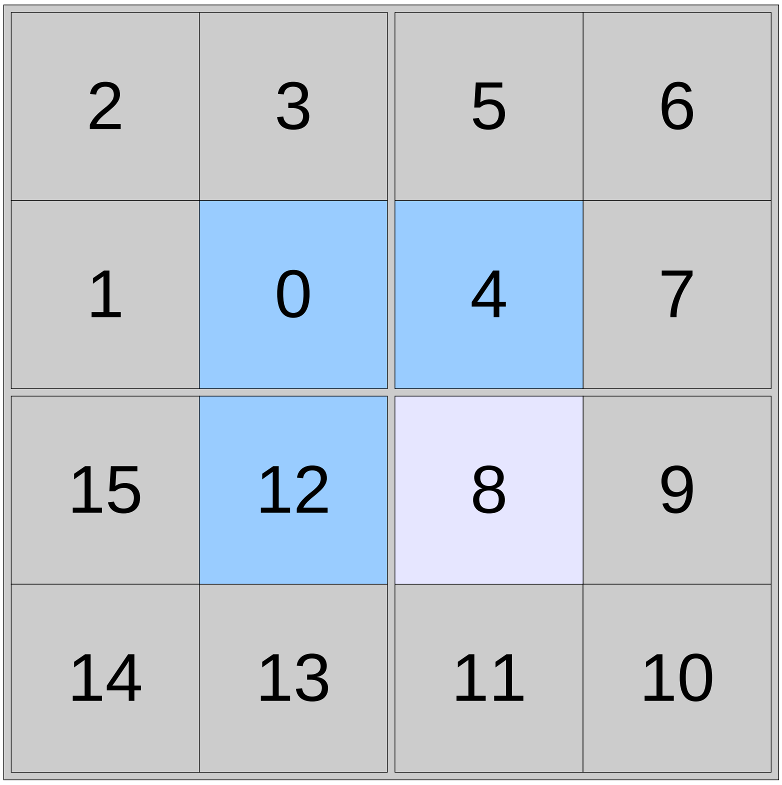

2	3	5	6
1	0	4	7
15	12	8	9
14	13	11	10

Figure C.1: Numbering scheme of the pads.

Appendix D

Energy resolution

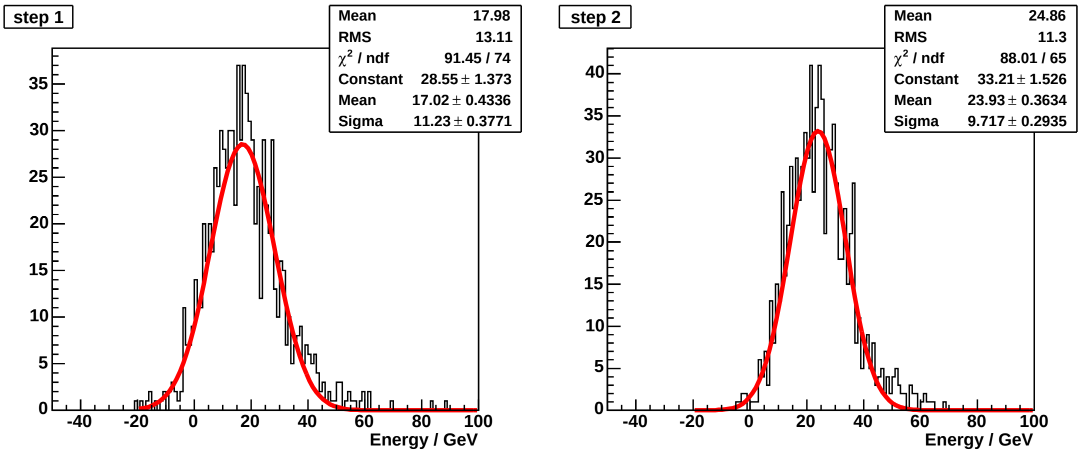

Figure D.1: Energy resolution for 30 GeV pion data.

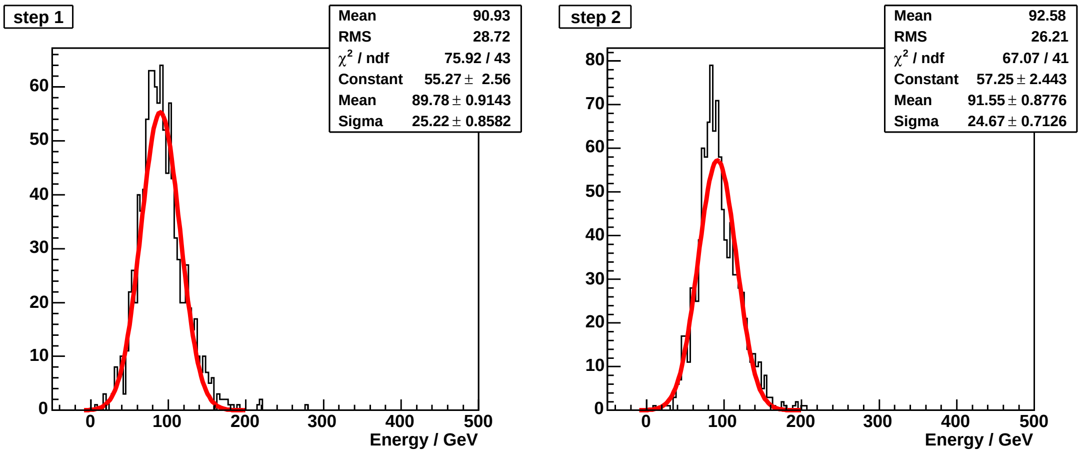

Figure D.2: Energy resolution for 100 GeV pion data.

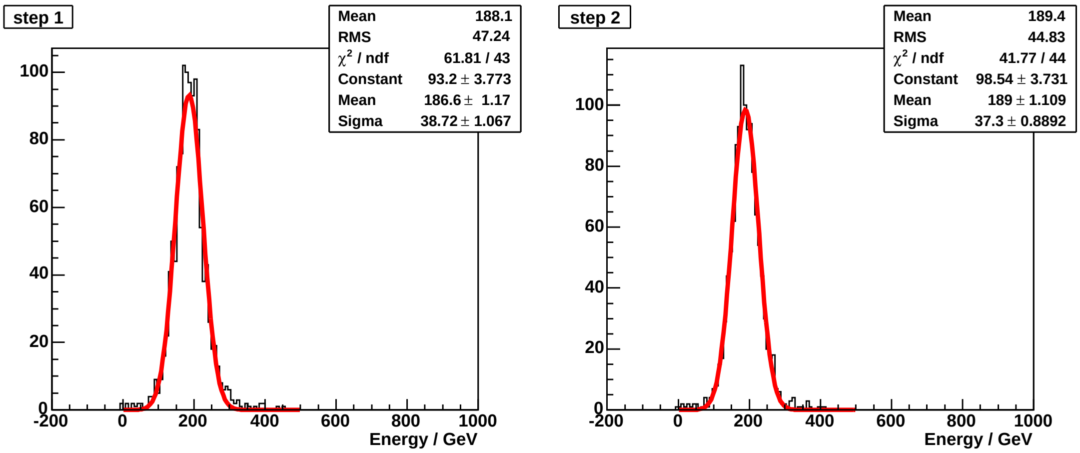

Figure D.3: Energy resolution for 200 GeV pion data.

Appendix E

Statistical subtraction of the noise events used for muon data

In order to determine the number of noise events in the signal, a Gaussian function is used to fit the signal distribution. The amplitude parameter divided by the width of the bin gives the number of noise events. The range, in which the distribution is fitted, is fixed, and this effects the amplitude parameter. Table E.1 gives the change in the number of noise events due to changes in the fit range of $\pm 1\sigma$ of the pedestal distribution.

Layer number	Number of noise events	-1σ	diff	$+1\sigma$	diff
1	3.20	2.88	10.13%	3.71	-15.85%
2	2.06	2.05	0.49%	2.26	-9.39%
3	1.96	1.99	-1.58%	2.09	-6.52%
4	2.03	2.12	-4.62%	2.24	-10.58%
5	3.36	2.94	12.51%	3.71	-10.56%
6	2.70	2.35	12.91%	3.03	-12.10%
7	2.21	2.05	7.31%	2.29	-3.83%
8	2.93	2.81	3.96%	3.31	-12.92%
9	4.94	4.36	11.59%	5.32	-7.79%
10	2.91	2.66	8.57%	3.22	-10.73%
11	2.31	2.31	-0.21%	2.47	-6.92%
12	2.81	2.54	9.36%	2.98	-6.27%
13	3.04	2.76	9.19%	3.40	-11.78%
14	2.40	2.06	14.15%	2.61	-8.44%
15	2.83	2.53	10.41%	3.20	-13.30%

Table E.1: Change in the number of noise events due to changes in the fit range of $\pm 1\sigma$ of the pedestal distribution. 100 GeV muon data have been used.

A global change of ±15% in the number of noise events has been chosen. The variation of the muon calibration constants due to these changes, is shown in table E.2.

Fit par. name	Fit par. value	-15%	diff.	$+15\%$	diff.
C_1	$9.53 \cdot 10^{-6}$	$9.53 \cdot 10^{-6}$	0.00%	$9.53 \cdot 10^{-6}$	0.00%
C_2	$8.61 \cdot 10^{-1}$	$8.62 \cdot 10^{-1}$	-0.15%	$8.60 \cdot 10^{-1}$	0.14%
C_3	1.27	1.28	-0.19%	1.27	0.18%
C_4	1.39	1.39	-0.16%	1.38	0.15%
C_5	$8.83 \cdot 10^{-1}$	$8.81 \cdot 10^{-1}$	0.16%	$8.84 \cdot 10^{-1}$	-0.18%
C_6	$7.98 \cdot 10^{-1}$	$7.97 \cdot 10^{-1}$	0.13%	$7.98 \cdot 10^{-1}$	-0.02%
C_7	1.21	1.21	-0.09%	1.21	0.08%
C_8	1.10	1.10	0.11%	1.10	-0.12%
C_9	$8.02 \cdot 10^{-1}$	$7.98 \cdot 10^{-1}$	0.59%	$8.07 \cdot 10^{-1}$	-0.62%
C_{10}	$3.81 \cdot 10^{-1}$	$3.81 \cdot 10^{-1}$	0.13%	$3.82 \cdot 10^{-1}$	-0.14%
C_{11}	$3.62 \cdot 10^{-1}$	$3.62 \cdot 10^{-1}$	-0.09%	$3.61 \cdot 10^{-1}$	0.08%
C_{12}	1.02	1.02	0.08%	1.02	-0.09%
C_{13}	1.22	1.22	0.12%	1.23	-0.13%
C_{14}	$1.47 \cdot 10^{-12}$	$2.44 \cdot 10^{-15}$	99.83%	$7.89 \cdot 10^{-12}$	-435.74%
C_{15}	fixed				
α	$1.33 \cdot 10^{2}$	$1.325 \cdot 10^{2}$	$1.344 \cdot 10^{2}$	0.72%	-0.72%
σ	$2.70 \cdot 10^{1}$	$2.700 \cdot 10^{1}$	$2.700 \cdot 10^{1}$	0.00%	0.00%

Table E.2: Changes in the fit parameters after the second step, due to changes of ±15% in the number of noise events. 100 GeV muon data have been used. The last layer is excluded from the analysis, therefore the C_{15} parameter is fixed to zero.

Appendix F

Statistical subtraction of the noise events used for pion data

A Gaussian function is used to fit the signal distribution. The amplitude parameter obtained from the fit, gives the number of noise events. Changing the range in which the function is fitted results in a change in the number of noise events. The variation obtained for changing the range by $\pm 1\sigma$ is given in table F.1 and F.2.

Hit pad

Number of noise events	-1σ	diff in %	$+1\sigma$	diff
1.55	1.34	13.33%	1.56	-0.81%
3.26	2.85	12.65%	3.29	-0.77%
7.81	5.93	24.10%	8.28	-6.02%
18.92	15.86	16.17%	20.01	-5.71%
47.18	40.75	13.61%	49.68	-5.30%
198.75	182.26	8.29%	203.88	-2.59%
513.36	490.60	4.43%	534.42	-4.10%
587.52	561.65	4.40%	643.50	-9.53%
712.52	705.03	1.05%	716.75	-0.59%
962.42	948.33	1.46%	964.67	-0.23%
1070.5	1059.0	1.08%	1070.9	-0.04%
1038.1	1056.8	-1.80%	1043.7	-0.54%
1278.3	1285.2	-0.53%	1281.0	-0.21%

Table F.1: Change in the number of noise events due to changes in the fit range, for the hit pad. 150 GeV pion data have been used.

Pad four

Number of noise events	-1σ	diff in %	$+1\sigma$	diff
29.35	26.61	9.33%	29.73	-1.31%
31.95	30.38	4.90%	32.13	-0.58%
54.91	48.23	12.17%	56.31	-2.55%
145.86	130.18	10.75%	148.27	-1.66%
207.51	194.47	6.29%	208.64	-0.54%
501.19	488.14	2.60%	527.83	-5.32%
533.36	497.74	6.68%	541.51	-1.53%
853.43	831.27	2.60%	863.09	-1.13%
923.87	901.68	2.40%	928.69	-0.52%
1051.4	1060.1	-0.82%	1059.0	-0.73%
1108.1	1128.5	-1.85%	1115.6	-0.68%
1007.1	1048.6	-4.12%	1013.6	-0.65%
1317.9	1345.3	-2.08%	1321.0	-0.24%

Table F.2: Change in the number of noise events due to changes in the fit range, for pad four. 150 GeV pion data have been used.

Appendix G

Position of beam spot

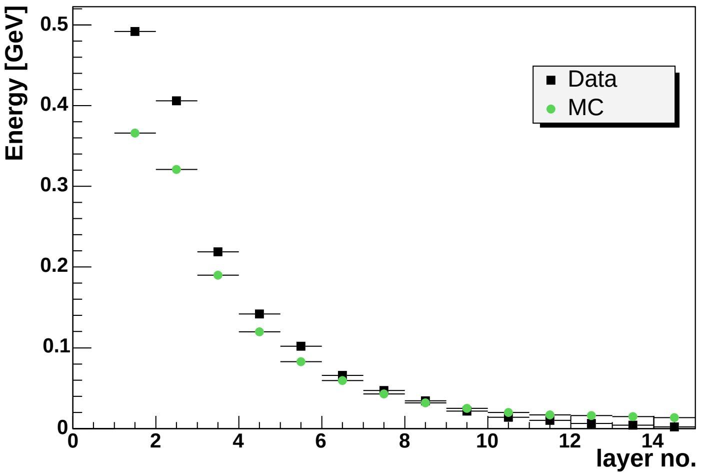

Figure G.1: Longidutinal energy distribution in the hit pad, obtained for 150 GeV pion data. The position of the beam in the MC is at **4 cm below** and **4 cm left** from the center of the layer.

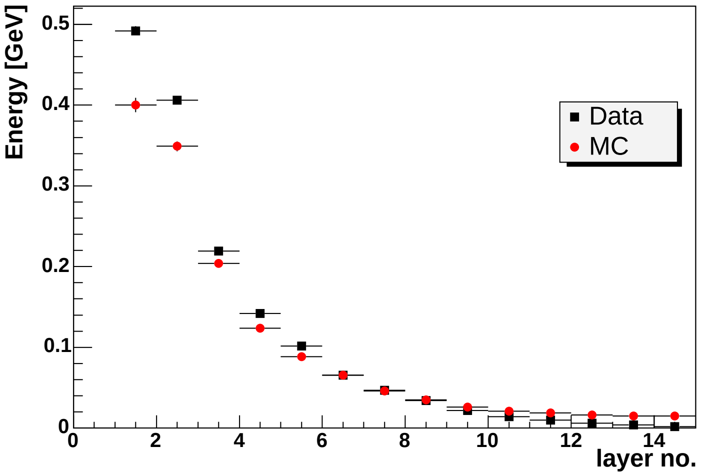

Figure G.2: Longidutinal energy distribution in the hit pad, obtained for 150 GeV pion data. The position of the beam in the MC is at **5 cm below** and **5 cm left** from the center of the layer.

Comparison between the normalized ratio

$$(E_{Data} - E_{MC})/E_{MC}$$

for beam 4 and 5 cm below and to the left of the center of the calorimeter.

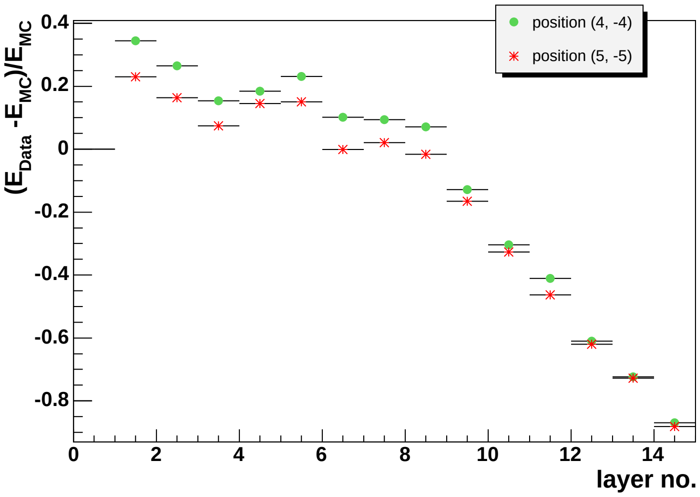

Figure G.3: Normalized difference between the energy reconstructed and the energy from MC for beam positions at **4 cm** and **5 cm** below and to the left of the center of the calorimeter.

Simulated data		Measured data	
E_{rec}	Error [%]	E_{rec}	Error [%]
$(3.66 \pm 0.03) \cdot 10^{-1}$	0.9	$(4.92 \pm 0.06) \cdot 10^{-1}$	1.1
$(3.21 \pm 0.02) \cdot 10^{-1}$	0.7	$(4.06 \pm 0.04) \cdot 10^{-1}$	1.1
$(1.90 \pm 0.01) \cdot 10^{-1}$	0.8	$(2.19 \pm 0.02) \cdot 10^{-1}$	1.1
$(1.20 \pm 0.01) \cdot 10^{-1}$	0.9	$(1.42 \pm 0.02) \cdot 10^{-1}$	1.4
$(8.26 \pm 0.09) \cdot 10^{-2}$	1.1	$(1.02 \pm 0.01) \cdot 10^{-1}$	1.4
$(5.96 \pm 0.08) \cdot 10^{-2}$	1.3	$(6.56 \pm 0.10) \cdot 10^{-2}$	1.5
$(4.29 \pm 0.07) \cdot 10^{-2}$	1.5	$(4.69 \pm 0.08) \cdot 10^{-2}$	1.7
$(3.19 \pm 0.06) \cdot 10^{-2}$	1.8	$(3.42 \pm 0.07) \cdot 10^{-2}$	2.1
$(2.49 \pm 0.06) \cdot 10^{-2}$	2.2	$(2.17 \pm 0.05) \cdot 10^{-2}$	2.4
$(2.00 \pm 0.05) \cdot 10^{-2}$	2.6	$(1.39 \pm 0.04) \cdot 10^{-2}$	2.7
$(1.70 \pm 0.05) \cdot 10^{-2}$	3.1	$(1.00 \pm 0.03) \cdot 10^{-2}$	3.3
$(1.58 \pm 0.06) \cdot 10^{-2}$	3.9	$(6.16 \pm 0.25) \cdot 10^{-3}$	4.0
$(1.45 \pm 0.07) \cdot 10^{-2}$	4.7	$(4.02 \pm 0.20) \cdot 10^{-3}$	4.9
$(1.36 \pm 0.07) \cdot 10^{-2}$	5.3	$(1.79 \pm 0.12) \cdot 10^{-3}$	7.0

Table G.1: Values of the energy reconstucted and simulated and the corresponding errors, for the hit pad, with the position of the beam at 4 cm below and 4 cm left from the center of the layer.

List of Figures

List of Tables

Bibliography

[Ant03] T. Antoni et al. (KASCADE Collaboration), *The cosmic ray experiment KASCADE*, Nucl. Instrum. Meth. **A513** (2003), 490–510.

[Aub93] B. Aubert et al. (WALIC Collaboration), *Studies of compensation of Fe/TMP and PB/TMP sampling calorimeters*, Nucl. Instrum. Meth. **A334** (1993), 383.

[Bie01] P. Biermann and G. Sigl, *Introduction to cosmic rays*, Lect. Notes Phys. **576** (2001), 1–26, astro-ph/0202425.

[Chi03] A. Chiavassa et al., *KASCADE-Grande: The Grande array*, Proc. 28th International Cosmic Ray Conference (ICRC 2003) (T. Kajita, Y. Asaoka, A. Kawachi, Y. Matsubara, and M. Sa saki, eds.), vol. 2, 2003, pp. 989–992.

[Dol02] P. Doll et al., *Muon tracking detector for the air shower experiment KASCADE*, Nucl. Instrum. Meth. **A488** (2002), 517–535.

[Eng96] J. Engler, *Liquid inonization chambers at room temperatures*, J. Phys. **G22** (1996), 1–23.

[Eng99] J. Engler et al., *A warm-liquid calorimeter for cosmic-ray hadrons*, Nucl. Instrum. Meth. **A427** (1999), 528–542.

[Fab85] C. Fabjan, *Calorimetry in high-energy physics*, CERN-EP/85-54 (1985).

[Fab03] C. Fabjan, *Calorimetry for particle physics*, Review of modern physics **75** (2003), 1243–1286.

[GEA93] *GEANT 3.15 Detector description and simulation tool*, CERN Program Library Long Writeup W5013 (1993).

[Gri01] P. K. F. Grieder, *Cosmic rays at earth: Researcher's reference, manual and data book*, Amsterdam, Netherlands: Elsevier (2001) 1093 p.

[Gro00] D. Groom et al. (Particle Data Group Collaboration), *Review of particle physics*, Eur. Phys. J. **C 15** (2000), 1–878.

[Gru00] see e.g. references in: C. Grupen, *Astroteilchenphysik*, Vieweg, Braunschweig/Wiesbaden, 2000.

[Hör94] J. Hörandel, *Kalibration von TMS-Ionisationskammern mit Myonen der Höhenstrahlung und Messung des Myonflusses*, Diplomarbeit, Universität Karlsruhe (1994).

[Hör04] J. Hörandel, *Private communication,* (2004).

[Kam03] K.-H. Kampert et al., *Status of the KASCADE-Grande experiment*, Nucl. Phys. Proc. Suppl. **122** (2003), 422–426, astro-ph/0212347.

[Leo87] W. Leo, *Techniques for Nuclear and Particle Physics Experiments*, Springer, Berlin, 1987.

[Mil00] J. Milke et al., *Calorimetry in High Energy Physics, G. Barreira, B. Tome*, Word Scientific p. 803, ISBN 981-02-4304-9 (2000).

[MIN98] *MINUIT 94.1 Function Minimization and Error Analysis*, CERN Program Library Long Writeup D506 (1998).

[Nag00] M. Nagano and A. A. Watson, *Observations and implications of the ultrahigh-energy cosmic rays*, Rev. Mod. Phys. **72** (2000), 689–732.

[Ple04] S. Plewnia, *Eigenschaften eines Kalorimeters mit Flüssigkeitsionisationskammern*, 2004, Given at DPG Frühjahrstagung, Fachverband Teilchenphysik, Mainz.

[Rao98] see e.g. references in: M. V. S. Rao and B. V. Sreekantan, *Extensive Air Showers*, World Scientific Publishing, 1998.

[Ruh96] W. Ruh, *Verstärkertechnik und elektronische Kalibration des KASCADE Kalorimeters*, Diplomarbeit, Universität Karlsruhe (1996).

[Wig00] R. Wigmans, *Calorimetry. Energy measurement in particle physics*, Clarendon Press, Oxford 2000.

Acknowledgement

I would like to thank all those who made this thesis possible.

First, I want to thank Prof. Dr. Peter Buchholz for giving me the opportunity to work on this interesting topic in the KASCADE-Grande experiment.

I would like to thank Prof. Dr. Claus Grupen for revising this thesis.

Special thanks to Dr. Wolfgang Walkowiak for guiding me through the steps of the analysis and for never running out of good ideas. I would also like to thank him for helpful comments during the writing of this thesis, especially during the last stages.

I thank Prof. Dr. Arif Mailov for finding solutions to my Fortran problems.

I would like to thank Jörg Hörandel, Jens Milke and Stefan Plewnia for assistance during the analysis.

I want to thank all members of our group for the nice time I had working with them.

Thanks for proof-reading to Ulrich Husemann, Kishore Ravuri, Irina Balescu, Sven Over and Valentin Sipica.

I want to thank Irina Balescu and Samer Hijazi, special friends who made the last year a wonderful time.

Finally, I want to thank my parents for loving and encouraging me for the last 25 years and to my brother who can always make me laugh.

Erklärung

Hiermit erkläre ich, dass ich die vorliegende Diplomarbeit selbständig verfasst und keine anderen als die angegebenen Quellen und Hilfsmittel benutzt, sowie Zitate und Ergebnisse Anderer kenntlich gemacht habe.

Tomaida-Roxana Lixandru